Simulations of extensional flow in microrheometric devices

Mónica S. N. Oliveira[a,b], Lucy E. Rodd[b,c], Gareth H. McKinley[b], Manuel A. Alves[a*]

[a]*CEFT, Departmento de Engenharia Química, Faculdade de Engenharia da Universidade do Porto, Rua Dr. Roberto Frias, 4200-465 Porto, Portugal*

[b]*Department of Mechanical Engineering, MIT, 77 Massachusetts Avenue, Cambridge , MA 02139-4307, USA*

[c]*Department of Chemical and Biomolecular Engineering, The University of Melbourne, VIC 3010, Australia*

Email**:** msno@mit.edu, l.rodd@uq.edu.au, gareth@mit.edu, mmalves@fe.up.pt

*****Corresponding author: tel. +351 225081680; fax +351 225081449

Acknowledgments: M.S.N.Oliveira would like to thank Fundação para a Ciência e Tecnologia (FCT), Portugal for financial support (SFRH/BPD/15005/2004, SFRH/BPD/34141/2006). M.A. Alves acknowledges the financial support provided under program POCI2010 by FCT and FEDER (project POCI/EQU/59256/2004)

We present a detailed numerical study of the flow of a Newtonian fluid through microrheometric devices featuring a sudden contraction-expansion. This flow configuration is typically used to generate extensional deformations and high strain rates. The excess pressure drop resulting from the converging and diverging flow is an important dynamic measure to quantify if the device is intended to be used as a microfluidic extensional-rheometer. To explore this, we examine the effect of the contraction length, aspect ratio and Reynolds number on the flow kinematics and resulting pressure field. Analysis of the computed velocity and pressure fields show that, for typical experimental conditions used in microfluidic devices, the steady flow is highly three-dimensional with open spiraling vortical structures in the stagnant corner regions. The numerical simulations of the local kinematics and global pressure drop are in good agreement with experimental results. The device aspect ratio is shown to have a strong impact on the flow and consequently also on the dimensionless excess pressure drop, which is quantified in terms of the dimensionless Couette and Bagley correction factors. We suggest an approach for calculating the Bagley correction which may be especially appropriate for planar microchannels with a contraction followed by an expansion and which may present a significant improvement in the approach presently used to analyze experimental data.

Keywords: Microfluidics, Microrheometry, Bagley Correction, Contraction-Expansion Flow, Extensional Flow

1. Introduction

Over the past decade, microfluidic devices have emerged as a powerful toolset for miniaturization and automation of fluid handling and fluid analysis (Whitesides 2006), significantly reducing the time and cost involved in diagnostic procedures. The numerous advantages of microfluidics, namely the reduced amounts of sample and reagents needed, the high surface-to-volume ratio, the substantial waste reduction, the low cost of fabrication and the possibility of producing highly integrated and disposable devices, have stimulated remarkable interest and unraveled an extensive range of applications in areas such as chemical technology and biotechnology: chemical reactors, sensors, flow control and flow focusing (as in inkjet printers), environmental monitoring, delivery of drugs and chemicals, isolation and tagging of biological material, in addition to analytical tools, which may be summarized as the "lab-on-a-chip" concept (Chow 2002; Stone et al. 2004; Nguyen and Wu 2005; Bayraktar and Pidugu 2006). As a result of the fabrication methods employed, micro-devices are typically composed of a series of planar channels and many of the geometries used involve changes in the cross sectional flow area (Lee et al. 2002a, 2002b). For this reason, understanding the effects of prototypical configurations, such as the planar contraction-expansion, is of utmost importance.

Viscous flow through contractions (planar and axisymmetric) is a long-standing numerical benchmark problem, particularly for viscoelastic fluids (Hassager 1988; Brown and McKinley 1994; Owens and Phillips 2002). This type of flow results in streamwise acceleration and is of particular importance in polymer processing applications, such as injection molding, spinning and film blowing (Barnes et al. 1989). The flow through sudden contractions, including the complex effects of flow geometry and fluid rheology on the flow characteristics, has been the subject of thorough reviews by Boger (1987) and White et al. (1987). More recent results (numerical and experimental) can be found in the book by Owens and Phillips (2002) and the introductions of Alves et al. (2005), Rodd et al. (2005) and Oliveira et al. (2007b).

Even though the geometry is simple, these entry flows show complex flow patterns that feature both shearing and elongational regions: near the walls the flow is shear-dominated, whereas along the centerline it is predominantly extensional and essentially shear-free (Rothstein and McKinley 2001). There are a considerable number of papers published both from an experimental (e.g. Durst et al. 1974; Cherdron et al. 1978) and numerical perspective (e.g. Drikakis 1997; Hawa and Rusak 2001; Oliveira 2003) considering Newtonian fluids (e.g.

Fearn et al. 1990; Drikakis 1997; Revuelta 2005) and non-Newtonian fluids (Townsend and Walters 1994; Mishra and Jayaraman 2002; Oliveira 2003; Poole et al. 2007). The flow through a sudden expansion can also exhibit quite complex behavior, even for laminar flows of Newtonian fluids (e.g. Fearn et al. 1990; Hawa and Rusak 2001; Mishra and Jayaraman 2002; Oliveira 2003) resulting in either symmetric or asymmetric streamline patterns depending on the value of the Reynolds number and on the geometrical characteristics (Battaglia et al. 1997).

At the microscale, entry flows are also important in many additional industrial applications from inkjet printing to micro-injection molding. These processes usually involve a strong extensional component: for example, inkjet printing, which is a high volume commercial industry, depends on the extensional flow of slightly elastic non-Newtonian fluids at the microscale (Oliveira et al. 2006; Tuladhar and Mackley 2007). The small length-scales of the geometries usually result in a range of Reynolds numbers well within the laminar flow regime. Furthermore, entry flows at the microscale are typically characterized by large contraction ratios, and thus both the extensional deformation rate and the total extensional strain are high. Consequently, a large additional pressure drop (or 'extra pressure drop') at the converging entrance is observed, even for Newtonian fluids, and this can be related to the extensional properties of the solution (Kang et al. 2005). A microfluidic geometry consisting of an abrupt contraction followed by an abrupt expansion may thus be used in order to determine an apparent extensional viscosity of dilute polymer solutions from pressure drop measurements in microcontractions (Scott 2004; Rodd et al. 2005). The underlying idea is to use streamwise acceleration of the fluid in the throat in order to achieve a local planar elongational flow in the core of the converging section, such that the velocity increases linearly towards the throat. If the contraction-expansion geometry is abrupt, spatially inhomogeneous extensional behavior is observed in the entrance region, and this can make it difficult to identify a single constant strain rate. The resulting material coefficient is therefore most accurately described as an "apparent extensional viscosity" (Rodd et al. 2005). Nonetheless, these microfluidic contraction-expansion flows are extensionally dominated and therefore important information can still be extracted from differential pressure measurements in a similar fashion to that performed in conventional contraction geometries (Cogswell 1972a, 1972b; James et al. 1990; Binding et al. 1998, 2006).

At the macroscale, the major flow pattern characteristic of Newtonian fluid flow through planar contraction geometries is the formation of an upstream Moffat vortex (Moffat 1964), close to the salient corner, which gradually diminishes as the effects of fluid inertia increase. For Newtonian fluids, the most interesting dynamical features of this flow take place in the expansion region. Early experimental studies of laminar flows through macroscale planar channels with a sudden expansion (Durst et al. 1974; Cherdron et al. 1978), revealed the existence of two recirculation regions of equal size downstream of the expansion for low Reynolds number flows. As the Reynolds number is increased, symmetry about the centerline is initially maintained and the recirculation length increases linearly (Durst et al. 1974; Cherdron et al. 1978). However, above a certain value of the Reynolds number, a supercritical bifurcation is observed and one recirculation zone expands while the other shrinks as the Reynolds number is further increased (Drikakis 1997; Revuelta 2005). Despite this asymmetry, the flow remains steady for a certain range of Reynolds number (Mishra and Jayaraman 2002). This phenomenon, in which stable asymmetric vortices are formed, is seen in 2D planar expansions and is attributed to the Coanda effect (Wille and Fernholz 1965). Infinitesimal perturbations of the velocity field cause the flow to be shifted to one side of the expansion, generating a velocity increase near one wall and a corresponding pressure decrease near that same wall. As a result, the flow asymmetry is likely to be maintained once the resulting pressure difference is established. The pattern of vortex development and growth has been observed experimentally and confirmed by a series of numerical studies (e.g. Wille and Fernholz 1965; Durst et al. 1974, 1993; Cherdron et al. 1978; Sobey and Drazin 1986; Drikakis 1997; Chiang et al. 2000; Oliveira 2003; Revuelta 2005). The numerical computations of Sobey and Drazin (1986) and Fearn et al. (1990) together with the linear stability analysis of Shapira et al. (1990) indicate that this behavior occurs as a result of a bifurcation in the solution to Navier-Stokes equations, i.e. above a critical Reynolds number two symmetric stable solutions co-exist (Battaglia et al. 1997). Hawa and Rusak (2001) explain the loss of symmetric stability as a result of the interaction between the effects of viscous dissipation, the downstream convection of perturbations by the base symmetric flow, and the upstream convection induced by two-dimensional asymmetric disturbances.

Oliveira (2003) predicted that, for Newtonian fluids in a 1:3 planar 2D expansion, the flow becomes asymmetric above a critical Reynolds number of $Re_c \approx 54$. This result is in good agreement with previous works (Shapira et al. 1990; Fearn et al. 1990; Drikakis 1997; Mishra and Jayaraman 2002). However this critical Reynolds number is found to depend strongly on

the expansion ratio, w_d / w_c, where w_c and w_d are the small and large channel widths respectively (Drikakis 1997; Revuelta 2005). Drikakis (1997) performed a numerical study of the laminar flow through sudden expansions with varying expansion ratios and found that the critical Reynolds number decreases with increasing expansion ratio and that the asymmetries become stronger with increasing Reynolds number. Furthermore, in 3D geometries, the critical Reynolds number varies with the aspect ratio, $AR = h / w_c$, where h is the depth of the channel in the "neutral" direction (Cherdron et al. 1978; Chiang et al. 2000).

An important difference in nomenclature must be noted here: at macroscales, a 'planar geometry' commonly refers to flow cells with large aspect ratios ($AR >> 1$) which are commonly used to approximate a 2D planar flow, i.e. the depth of the channel is designed to be large ($h / w_c >> 1$) so that the effects of the endwalls are negligible. When the aspect ratio decreases, the effects of the endwalls increase; in expansion flows, for example, the critical Reynolds number for the bifurcation increases, and eventually the flow patterns observed experimentally no longer become asymmetric at large Reynolds numbers (Chiang et al. 2000). For moderate aspect ratios, the flow is highly three-dimensional, and complex spiraling vortical structures are observed, which are not closed recirculating cells as in the case of ideal 2D expansion flows. By contrast, in lithographic microfabrication techniques, the term 'planar geometry' typically refers to devices in which the depth, h, of the flow channel is kept constant throughout the device and changes to the cross-sectional flow area (such as a contraction and/or expansion) occurs only in the flow direction. This typically leads to aspect ratios close to unity in the contraction region ($AR = h / w_c = O(1)$) and much smaller aspect ratios upstream and downstream of the region of interest ($h / w_d << 1$). Steady viscous flow in microfluidic devices should thus be expected to be three-dimensional in nature. Tsai et al. (2006) examined the flow of Newtonian fluids through microfabricated planar expansions numerically and found that the flow only resembles a two-dimensional flow for very high aspect ratios ($AR = h / w_c >> 1$); otherwise near the expansion plane the flow is locally three-dimensional. The theoretical study of Lauga et al. (2004) shows that even for low aspect ratios ($AR < 1$) the flow is highly three-dimensional, a result that is more important whenever there are abrupt changes in the cross-section of the geometry.

The pressure drop is an important dynamical quantity associated with viscous flow through channels having sudden changes in cross-sectional area. In entry flows, the total pressure drop is composed of two parts, one caused by the pressure drop over the length of the channel due

to fully-developed viscous flow plus an excess pressure drop that arises from the entrance and exit effects. The latter component results from streamwise deformations associated with characteristic features like contractions and expansions and may represent a significant portion of the total pressure drop, even in the case of Newtonian fluid flows (Kang et al. 2005, 2006; Oliveira et al. 2007a), particularly when a short contraction channel is used. This extra pressure drop is difficult to measure directly by experimental means (Kang et al. 2006) and is usually presented in terms of a dimensionless Couette correction or a Bagley correction (Bagley 1957; Boger 1982) obtained by extrapolating experimental measurements. These "end effects" originate mainly from the streamwise rearrangement of the velocity profile and the resulting extensional flow (Kang et al. 2006), therefore the excess pressure drop yields information about the global state of viscoelastic stresses in the flow (Rothstein and McKinley 2001). In fact, many researchers have attempted to use the excess pressure as a means to estimate the extensional viscosity of viscoelastic fluids and approximate analysis are often used (Cogswell 1972a; Binding et al. 1988; Boger and Binnington 1990; James et al. 1990; Rothstein and McKinley 2001; Rodd et al. 2005).

The ultimate goal of this research is to develop an efficient microfluidic "rheometer-on-a-chip" capable of achieving high strain rates, in such a way that can be used to measure the effective extensional properties of dilute polymeric solutions and low viscosity complex fluids (e.g. inks, polymeric surfactants, coating fluids, DNA solutions, blood). In this paper we investigate the flow of a Newtonian fluid (distilled water) through a microfabricated geometry containing a planar contraction-expansion section. We combine experimental measurements with numerical computations to obtain accurate velocity profiles, flow patterns and vortex sizes as well as pressure drop results. As we show below, excellent agreement can be obtained between the experimental and numerical techniques, validating the use of future numerical computations as an exploratory design tool. The present study is a starting point for a more in-depth numerical study of the flow of viscoelastic fluids in these types of micro-geometries. However, as we shall demonstrate, even for a simple Newtonian fluid the flow in such a device can be complex and is yet to be completely understood.

The paper is organized as follows. In Section 2, we describe the experimental geometry, method of fabrication and the experimental techniques used for the measurements. In Section 3, the governing equations and the numerical method used to solve them are summarized. The flow geometry and the computational meshes used are also outlined. The

experimental and numerical results are discussed in Sections 4 to 6: the global flow field and vortex characteristics are analyzed in Section 4; in Section 5 a detailed study of the velocity field is carried out; and in Section 6 the corresponding pressure drops are evaluated. Finally, in Section 7 we summarize the main conclusions of this work.

2. Experimental

2.1 Channel Geometry and Fabrication

The channels were fabricated in polydimethylsiloxane (PDMS) from a SU-8 photoresist mold using standard soft-lithography techniques (McDonald et al. 2000; Ng et al. 2002). The master molds were prepared using a high-resolution chrome mask together with a contrast enhancer and a barrier coat to allow for smooth, nearly-vertical walls and sharp, well-defined corner features. Each set of PDMS channels was bonded permanently to a microscope cover slip after being air plasma treated. A detailed description of the experimental channel fabrication outlined above can be found in Scott (2004) and Rodd et al. (2005).

A sketch of the micro-geometry used in this work is presented in Figure 1. The set of channels was designed to have approximately a 16:1:16 contraction-expansion ratio and different contraction lengths were tested: L_c = 100, 200 and 400 μm. In all cases, the channel depth, h = 55 μm, the width of the upstream and downstream channels, $w_u = w_d$ = 400 μm, and the contraction width were kept constant. The mask used to produce the channels resulted in a final contraction width of w_c = 26 μm (as determined by profilometry) instead of the targeted 25 μm required to achieve the 16:1:16 contraction-expansion ratio; so in effect we have a 15.4:1:15.4 ratio. The point located at the centerline of the contraction plane and midway between each end-wall is taken as the coordinate origin ($x = y = z = 0$). The length of the upstream and downstream channels is long enough that the flow reaches a fully-developed velocity profile at all flow rates studied.

Pressure taps were located 3 mm upstream and downstream of the contraction plane (z = 0). A constant displacement-rate syringe pump (Harvard Apparatus PHD2000) was used to impose a constant flow rate into the micro-device 10 mm upstream of the contraction plane, over a wide range of flow rates $0.1 \leq Q \leq 8$ ml/h. A brief description of the experimental

configuration and procedures is given below; further details can be found in Rodd et al. (2005).

2.2 Flow Visualization and Velocity Measurement

The steady flow kinematics were characterized experimentally using fluorescent streak imaging and micro particle image velocimetry (μPIV). For the streak imaging, the fluid was seeded with 1.1 μm diameter fluorescent particles (Ex/Em = 520/580 nm) at a weight concentration of 0.02%. A 3.5 MP Apogee Instruments CCD camera (2184 × 1472 pixels) with a 30 ms exposure time was used to acquire the images. This camera was connected to a Nikon TE2000-S inverted microscope with an epi-fluorescence attachment (MVI Instruments) and a 10X objective with numerical aperture NA = 0.3. The flow was illuminated with a mercury light in combination with a dichroic mirror and filter set in order to isolate the 546 nm peak of the mercury lamp light spectrum, and the resultant particle fluorescence signal (580 nm). For the set-up used the depth of measurement corresponds to 29.7 μm, which amounts to 54 % of the channel depth in the observable streak line images (Rodd et al. 2005).

The μPIV technique uses the basic PIV principle of measuring the local velocities from the average displacement of tracer particles in a correlation region over a known time (Wereley and Meinhart 2004). Fluorescent particles (Molecular Probes, Ex/Em = 520/580 nm) with 0.5 μm diameter were added to the fluid at a concentration of 0.05% and a double-pulsed 532 nm Solo Nd:YAG laser system (New Wave Research) was used to illuminate the flow. A digital CCD camera (1.4MP PCO Sensicam; 1375 × 1040 pixels) connected to the Nikon microscope with a 20X objective lens (NA = 0.5) was used to capture the resulting images of particle displacement. In this configuration, the measurement depth is 11.7 μm, which corresponds to 21% of the channel depth (Oliveira et al. 2007a). In order to optimally resolve the velocities in the section to be analyzed, the time separation (δt) between individual images was varied depending on the flow rate used, so that the particle displacements (along the centerline) were within the range $1.5d_p \leq \delta z \leq 8d_p$, where d_p is the particle diameter and δz is the particle displacement. For each experiment, a set of 25 image pairs were recorded, processed and ensemble averaged using Insight 6.0 software package from TSI. Each image was cross-correlated in interrogation areas of 32 × 32 pixels using a Nyquist algorithm with a 50% overlap to generate two-dimensional velocity vector maps. A detailed discussion on the resolution and accuracy of the μPIV technique is presented in Oliveira et al. (2007a).

2.3 Pressure Drop Measurement

The pressure drop was measured experimentally across a section of the channel containing the contraction-expansion. For this purpose, we used solid-state differential pressure sensors (Honeywell 26PC) connected via flexible tubing to two pressure taps located 3 mm upstream and downstream of the contraction plane.

3. Numerical Simulations

3.1 Governing Equations and Numerical Method

The governing equations for an isothermal incompressible fluid flow are the conservation of mass and momentum, expressed as follows:

$$\nabla \cdot \mathbf{u} = 0 \tag{1}$$

$$\rho\left[\frac{\partial \mathbf{u}}{\partial t} + \nabla \cdot \mathbf{uu}\right] = -\nabla p + \nabla \cdot \boldsymbol{\tau} \tag{2}$$

where ρ is the density of the fluid, t the time, $\mathbf{u}$ the velocity vector, p the pressure and $\boldsymbol{\tau}$ the extra stress tensor.

An appropriate constitutive equation is needed for $\boldsymbol{\tau}$. Since in this work we are interested in Newtonian fluid flows, then

$$\boldsymbol{\tau} = \mu\left(\nabla \mathbf{u} + \nabla \mathbf{u}^{\mathrm{T}}\right) \tag{3}$$

where μ is the viscosity.

In Newtonian calculations Eq. (3) is usually substituted in Eq. (2) and the well-known Navier-Stokes equations are then obtained. However, the numerical code used in this work has been

developed especially for differential viscoelastic models (of which Eq. (3) is a particularly simple limiting explicit case) and as such we keep Eq. (3) separated from Eq. (2), as in previous works (e.g. Oliveira et al. 1998; Oliveira and Pinho 1999). For all practical purposes this separation makes no difference, except for the additional memory used to allocate storage for the extra stress tensor. For a comparison between the formulation used in this work and the classical approach using Navier-Stokes equations see the work of Oliveira and Pinho (1999).

Equations (1) to (3) assume the validity of the continuum hypothesis, an assumption which has been questioned in a number of works related to microfluidic applications (Pit et al. 2000; Barrat and Bocquet 1999). Some preliminary experiments involving liquids in lyophobic channels have observed slip occurring at the solid boundary (see review by Neto et al. 2005 and references therein). However, as far as current techniques permit, for Newtonian liquid flows at the micrometer length scales it has been well established that under standard conditions the basic laws governing fluid flow, expressed by the conservation of mass and momentum equations and the no-slip boundary condition at the walls, remain valid (Whitesides and Stroock 2001; Koo and Kleinstreuer 2003; Sharp and Adrian 2004; Rodd et al. 2005; Karniadakis et al. 2005). For water, the continuum assumption is not expected to break down when the channel dimensions are above 1 μm (Gad-el-Hak 2002). In fact, a 10 μm thickness channel contains about 3×10^4 water molecules (considering a diameter of ≈ 0.3 nm for a water molecule), enough to treat the flow under the continuum theory (Bayraktar and Pidugu 2006). The agreement between experimental results and the numerical simulations here presented provides further credibility to this assumption.

A finite-volume method is used to solve Eqs. (1) - (3) numerically, using a time marching algorithm (Oliveira et al. 1998; Alves et al. 2000). In this methodology, the resulting algebraic equations relate the dependent variables (p, $\mathbf{u}$, $\boldsymbol{\tau}$), which are calculated at the center of the cells forming the computational mesh, to the values in the nearby surrounding cells. Orthogonal non-uniform block-structured meshes are used to map the computational domain. Since we are dealing with steady-state calculations, the precision in the time derivative is not so important and therefore we use an implicit first-order Euler scheme. Central differences are used to discretize the diffusive terms, while the CUBISTA high-resolution scheme (Alves et al. 2003) is used in the discretization of the advective terms of the momentum equations. This scheme is based on the QUICK scheme of Leonard (1979) and maintains its third-order

accuracy while ensuring boundedness and good iterative-convergence properties (Alves et al. 2003, 2004).

The physical properties of the fluid used in the numerical calculations were selected to match those measured experimentally, i.e. the viscosity was set to 0.94 mPa·s and the density to 998 kg·m^{-3}.

3.2 Problem Definition and Dimensionless Numbers

In order to be able to capture the flow asymmetries expected at large *Re* the full domain is used in the simulations, i.e., no symmetry boundary conditions are imposed. The geometry used for the computations is the same as in the experiments, as illustrated in Figure 1. The dimensions of the inlet and outlet lengths were set to be longer ($L_u = L_d = 30w_u$) than the experimental device to ensure that the flow fully develops upstream of the contraction and completely re-develops downstream of the expansion. This is also required in order to obtain precise values of the excess pressure drop due to the presence of the contraction-expansion. Three different contraction lengths were simulated to match experiments: L_c = 100, 200 and 400 μm. As mentioned in the Introduction, there are two important geometrical ratios to be considered in contraction-expansion flows: the aspect ratio and the contraction ratio (or expansion ratio). The contraction ratio is defined as $CR = w_u / w_c$ and was kept constant throughout this study to match the experimental conditions described in Section 2.1. The aspect ratio is defined as $AR = h / w_c$. In the experimental study, a single channel depth of h = 55 μm was used, while in the numerical simulations, the depth of the channel was varied from 0.1 μm to 800 μm, i.e. the aspect ratio was varied by almost four orders of magnitude, in order to analyze its influence on the resulting flow kinematics and on the pressure drop. The limiting case of 2D flow ($AR \rightarrow \infty$) is also analyzed in detail. In this case only one cell in the *y*-direction is used, with symmetry boundary conditions imposed in both faces. This is the usual procedure used in our 3D-finite volume code for performing 2D flow calculations.

The other important dimensionless variable that characterizes the flow behavior of an incompressible Newtonian fluid is the Reynolds number. Control volume analysis of fully-developed flow leads to the concept of a hydraulic diameter described in terms of the cross-sectional area and wetted perimeter of the channel cross section: $D_h = 4\,\text{Area/Perimeter}$ (Gad-el-Hak 2002). This quantity provides a simple way of characterizing a channel of non-

circular cross-section using a single characteristic length scale. In microfluidics, where we are commonly dealing with channels of planar cross-section, it is typical to define the Reynolds number as a function of the hydraulic diameter of the contraction channel, $D_{h,c} = 2h\,w_c/(h+w_c)$, and the average velocity in the same contraction region ($<V_z>_c = Q/h\,w_c$, where Q is the volumetric flow rate) (Rodd et al. 2005; Tsai et al. 2006) resulting in:

$$Re = \frac{\rho <V_z>_c D_{h,c}}{\mu} = \frac{\rho <V_z>_c w_c}{\mu}\frac{2AR}{AR+1} \tag{4}$$

For 2D flows, in which $h / w_c >> 1$, $D_{h,c} \to 2\ w_c$ and the Reynolds number becomes

$$Re_{(2D)} = \frac{2\rho <V_z>_c w_c}{\mu} \tag{5}$$

Alternatively, the Reynolds number can be defined directly in terms of the contraction width:

$$Re_{w_c} = \frac{\rho <V_z>_c w_c}{\mu} \tag{6}$$

i.e. $Re_{w_c} = Re\ \frac{AR+1}{2AR}$, which in some cases can be a more convenient representation of the flow behavior, as will be discussed in Section 6.

3.3 Computational Meshes

Computational meshes with different levels of refinement were used to map the contraction-expansion geometry characterized by L_c = 100 μm and h = 55 μm: Mesh M1 had a total of 93 120 cells (NC) and Mesh M2, obtained by doubling the number of cells in each direction, is composed of 744 960 cells. Figure 2 shows a zoomed view of mesh M2 near the contraction region. The meshes are orthogonal but non-uniform. The smallest control volumes are concentrated near the re-entrant corners, where stress and velocity gradients are expected to be higher, as illustrated in the zoomed inset in Figure 2.

Table 1 shows the major characteristics of meshes M1, M2 and additional meshes used in the numerical studies for 3D simulations. These additional meshes are based on M1: varying the number of cells in the out-of-plane direction as a function of the channel depth (M5, M6, M7); and/or varying the number of cells in the contraction along the axial direction as a function of the contraction length (M3 and M4).

Table 1. Main characteristics of the three-dimensional computational meshes

Mesh	L_c (μm)	h (μm)	NC	$\Delta x_{\min} / w_c$	$\Delta y_{\min} / w_c$	$\Delta z_{\min} / w_c$
M1	100	55	93 120	0.04	0.04	0.04
M2	100	55	744 960	0.02	0.02	0.02
M3	200	55	95 680	0.04	0.04	0.04
M4	400	55	99 264	0.04	0.04	0.04
M5	200	100	143 520	0.04	0.04	0.04
M6	200	400	287 040	0.04	0.04	0.04
M7	200	800	478 400	0.04	0.04	0.04

For the flow conditions studied using 3D numerical simulations (0.1 ml/h $\leq Q \leq$ 12 ml/h), the effect of mesh refinement can be assessed from the axial velocity profiles and contour plots presented in Figure 3. There is little difference between the results obtained with each mesh at either flow rate, with a maximum relative error of 1.5% in the axial velocity. Similar results were found for other variables and therefore, unless stated otherwise, the results presented in the remainder of the paper were obtained with the coarser mesh M1. In the limiting 2D case, where we study a much broader range of flow rates, the effect of mesh refinement can be more noticeable at higher Reynolds numbers. Also, to be able to capture accurately the critical conditions for onset of flow asymmetries and bifurcations, meshes with high spatial refinement are necessary. Therefore, the 2D results presented in this work were computed with meshes M8 through to M11 which are more refined in the *x*-*z* plane than meshes M1-M7, as can be assessed from Table 2.

Table 2. Main characteristics of the two-dimensional computational meshes

Mesh	L_c (μm)	NC	$\Delta x_{\min} / w_c$	$\Delta z_{\min} / w_c$
M8	200	45 528	0.02	0.02
M9	200	182 112	0.01	0.01

M10	400	46 808	0.02	0.02
M11	400	187 232	0.01	0.01

4. Flow Patterns and Vortex Characteristics

In this section, we examine the global characteristics of the flow of a Newtonian fluid through a microscale sudden contraction followed by a sudden expansion. We begin by analyzing the effect of the Reynolds number on the flow patterns and vortex length for the microfluidic geometry used in the corresponding experiments ($L_c = 200$ μm, $CR = 15.4$ and $AR = 2.12$). The numerical calculations and the experimental results are compared directly, and we subsequently perform a numerical analysis of the effect of the aspect ratio on the fluid flow patterns and vortex length. To finalize, 2D flow patterns are shown and onset of flow asymmetries are discussed.

4.1 Experimental Microfluidic Device (3D Computations)

At low flow rates the diverging flow downstream of the expansion plane is symmetric as shown in Figure 4. In this figure we overlay the experimental streak lines measured at the center plane ($y = 0$) downstream of the expansion plane with the corresponding numerical calculations. There is a good agreement between the experimental streak lines and the numerical predictions, which can be further confirmed in Figure 5. An increase in the Reynolds number leads to the development and enhancement of "lip vortices" ($Re \lesssim 20$), as well as reattached symmetric corner vortices at higher Reynolds number ($20 \lesssim Re \lesssim 60$), downstream of the expansion plane (Figure 4). This is in agreement with the observations of Townsend and Walters (1994), for a 14:1 expansion geometry, and Rodd et al. (2005), for a similar geometry to the one used here. In Figure 5, we illustrate the effect of inertia on the size of the primary vortices formed downstream of the expansion as the Reynolds number is increased. The dimensionless size of the lip vortex that is formed at low Re is defined by its length in the x-direction normalized with w_u (L_{lip} / w_u, see Figure 4) and is limited to a maximum of $(w_u\text{-}w_c)/(2w_u) = 0.47$. Vortex enhancement occurs as the effects of inertia increase and once they reach the salient corner, the vortices continue to grow in the downstream direction. Their size (L_V) is now parameterized by the vortex length in the z-direction as illustrated in Figure 4 (and by convention they are now termed corner vortices). It should also be noted that the streak lines and vortex sizes measured experimentally are

symmetric about the centerline even for the highest Reynolds number tested. A small but systematic discrepancy between experiments and simulations can be seen for the higher flow rates ($Re \gtrsim 30$), manifested in an underestimation of the predicted vortex length (cf. Figure 5). This difference in vortex size can be explained by considering propagation of experimental uncertainty into the reported Reynolds number. This uncertainty is due to a combination of errors (on density, viscosity, flow rate or channel dimensions). To clarify this issue, we compare streamlines (projected on the center plane, $y = 0$) obtained numerically by keeping the flow rate constant and varying the depth of the channel from 50 to 60 μm, (corresponding approximately to a $\pm 9\,\%$ variation relative to the measured depth and an associated $\pm 6\,\%$ variation on *Re*). This is shown in Figure 6 for a flow rate of 6 ml/h ($Re = 46.6$, 43.7 and 41.2 for $h = 50$, 55 and 60 μm, respectively) and $L_c = 200$ μm. Errors of ≈ 10% in the size of the vortex and in the corresponding streak lines arise; for perfect overlap between calculation and experiment, the Reynolds number used in the numerical simulations needs to be only 6% lower.

At first glance, the experimental streak lines and the numerical predictions in Figure 6 may suggest that the recirculations are closed structures. In fact, in a 3D geometry, the presence of a top and bottom bounding wall leads to complex three-dimensional spiraling recirculation structures (Chiang et al. 2000; Tsai et al. 2006). This is highlighted by the *projected streamlines* in Figures 7a and b, at the center plane and near the out-of-plane wall, respectively. The fluid enters the vortical structure close to the wall and follows a spiral movement towards the center plane, where it exits the recirculation. Nevertheless, despite the different circulation patterns and the fact that the flow is highly three-dimensional, the sizes of the projected streamlines near the wall and at the center plane are very similar. Thus, even though the experimental streak line images cover approximately 54% of the channel depth (as explained in Section 2.2), they are visually very clear and sharp.

The complex path of two fluid elements in a 3D geometry is illustrated in Figure 8a, where the open nature of the recirculation is clearly evident. To obtain the streak lines displayed, the two fluid elements were selected in order to pass a point downstream of the contraction with the same axial and lateral coordinates, $z = 500$ μm and $x = 180$ μm, but with different out-of-plane coordinates: $y = 1$ μm (1 μm from the center plane; *fluid element 1*) and $y = 26.5$ μm (1 μm from the wall; *fluid element 2*). In this way, we capture one of the particles that is entrained within the recirculation and another one that just manages to avoid it. An analysis of

the Lagrangian trajectories of the two particles (Figure 9) shows a large difference in residence times. Even though *fluid element 2* spends most of the time close to the upper bounding wall, where the velocities are lower, its residence time is smaller since it is not trapped in the recirculation. Figure 8b illustrates the time evolution of the velocity magnitude corresponding to the fluid elements represented in Figure 8a. For each material element the velocity peaks as the fluid enters the contraction, but the maximum velocity reached is lower for the particle that enters the recirculation (*fluid element 1*), since at this point the particle is closer to the wall than *fluid element 2* (cf. Figure 9c). As *fluid element 1* exits the contraction, it is caught in the recirculation and the velocity magnitude is seen to increase and decrease cyclically as the fluid element moves towards and then away from the lateral wall, respectively. The maximum velocity magnitude for each loop increases gradually as the fluid element moves away from the upper wall and closer to the center plane. The recirculation loop with the highest velocity occurs for later times, close to the point when the particle exits the recirculation. Contrary to the pattern exhibited by *fluid element 1*, *fluid element 2* avoids becoming entrained in the recirculation when it exits the contraction. Consequently, it remains close to the upper wall and the velocity magnitude does not vary significantly as it flows steadily downstream.

4.2 Effect of the Aspect Ratio

In such a markedly three-dimensional flow, the channel depth is bound to have an impact on the flow patterns. Figure 10 illustrates the effect of varying the aspect ratio AR on the predicted streamlines. The numerical calculations were obtained for L_c = 200 μm, keeping the Reynolds number constant (Re = 43.7, as defined in Eq. (4)) while varying the channel depth h. The primary vortices are seen to expand as the channel depth is increased, while keeping the Reynolds number constant. It is interesting to note that, for this chosen value of Re, the flow becomes asymmetric at an aspect ratio ($AR = h / w_c$) between 100/26 and 400/26. Thus, by reducing the strength of secondary flows and inhibiting the onset of flow asymmetries, the walls have a stabilizing effect on the flow patterns. It is important to notice that we only observe asymmetries at rather high aspect ratios (of about 16 and higher) for the Reynolds number analyzed. For the 3D geometry used in the experiments ($AR = h / w_c = 2.12$) no asymmetries were observed even for a Reynolds number as high as 109.2.

With the objective of performing a systematic study of the effect of the aspect ratio on the flow structure, we have carried out an extensive set of simulations and classified the patterns of the flow downstream of the contraction at increasing Reynolds number. These calculations were performed for $L_c = 400$ μm and the resulting flow structures were classified as "no vortex", "lip vortex", "corner vortex", "combination of lip and corner vortices", "full corner vortex" and "asymmetric flow structure". The vortex pattern map in Figure 11 illustrates these flow structures and their location in a two-dimensional $\mathcal{H}$ - Re parameter space. We have chosen the dimensionless variable $\mathcal{H} \equiv h / (h+w_c) = AR / (AR+1)$ as the appropriate geometric ratio to plot, instead of the raw aspect ratio AR defined previously, so the values of the ordinates are bound between zero ($AR \to 0$; corresponding to the Hele-Shaw flow limit) and unity ($AR \to \infty$; corresponding to the 2D flow limit).

In the lower left corner of Figure 11, which represents low $\mathcal{H}$ and low Re, there is no visible vortex formation downstream of the expansion and the flow patterns resemble that of irrotational flow. On the other hand, in the opposite corner of high $\mathcal{H}$ and high Re, asymmetric flow with large vortical structures, is observed. Inbetween these two regions, we find a combination of lip and/or corner vortices. Independently of its nature, vortex enhancement with inertia is seen for all aspect ratios considered except in the limit of $\mathcal{H} \to 0$, for which we have a Hele-Shaw flow, and therefore the flow in the z-x plane is irrotational. The formation of a small and weak vortex near the salient corner, appears to occur at a fixed value of $\mathcal{H} \approx 0.5$ (corresponding to $AR \approx 1$) independently of the Reynolds number. Increasing the Reynolds number leads to the onset of a lip vortex, near the re-entrant corner, which increases in size and intensity until it reaches the downstream wall, creating a large corner vortex. Further increasing Re leads to flow asymmetry at high $\mathcal{H}$ as already discussed.

4.3 Two-Dimensional Geometry (2D)

As noted in the Introduction, the fluid motion approaches a truly two-dimensional flow when $AR >> 1$ (Chiang et al. 2000; Tsai et al. 2006), and is prone to develop asymmetries in the downstream channel as the Reynolds number increases (e.g. Oliveira 2003). In Figure 12, we examine the onset of these asymmetries in more detail by showing the streamlines calculated

numerically for 2D flow as a function of *Re*. The Reynolds number in the 2D geometry is given by $Re_{(2D)} = \rho \langle V_z \rangle_c \, 2w_c / \mu$, as already explained in Section 3.2. It should be noted that many authors studying 2D flows in expansion geometries prefer to use $Re = \rho \langle V_z \rangle_c \, w_c / \mu$, which is half of the value reported here. For low Reynolds number (e.g. $Re_{(2D)} = 0.01$), the viscous flow through the contraction-expansion geometry is reversible as shown in Figure 12 and it is impossible to distinguish the flow direction. For $Re_{(2D)} = 1.3$ (Figure 12b), the small Moffat vortex upstream of the contraction reduces slightly, while the vortex downstream of the expansion plane increases in size and intensity. It is clear that in the limiting case of a 2D geometry, the vortices are now closed-loop structures. The flow remains symmetrical about the center plane ($x = 0$), as the Reynolds number is further increased, and in addition the corner vortices downstream of the expansion grow while the upstream corner vortices get smaller, as indicated by the streamline plots in Figures 12b-c. On further increasing $Re_{(2D)}$, we find that the 2D flow exhibits a supercritical bifurcation, which is typical of 2D expansion flows (see Oliveira 2003 and references therein), becoming asymmetric with respect to the *z*-direction. At $Re_{(2D)} = 71.3$ (Figure 12e), a third large vortex has already emerged downstream of the expansion.

The evolution of the vortex structure can be summarized in Figure 13, in which we show the effect of the Reynolds number on the size of the vortices formed downstream of the 2D planar expansion. The lengths corresponding to each branch of this bifurcation diagram (L1 to L4) are marked in Figure 12e. The critical Reynolds number for the onset of asymmetric flow is approximately $Re_{(2D)_c} \approx 28.5$. At $Re_{(2D)} = 31.1$ the flow is clearly asymmetric (Figure 12c), but for $Re_{(2D)} = 28.5$, although not yet clearly visible in the bifurcation plot, a slight asymmetry is already present. This value is in good agreement with the computed results of Mishra and Jayaraman (2002) in a 1:16 two-dimensional expansion ($Re_{(2D)_c} = 25.2$), even though the two works are not exactly comparable (here the contraction/expansion ratio is actually $CR = 15.4$ and the flow in the smaller channel may not be fully developed when the expansion is approached). Near the critical point, the larger recirculation increases in size while the smaller one decreases as the Reynolds number increases. For $Re_{(2D)} \approx 42$, a new vortex forms downstream of the two primary vortices (Figure 12e) on the side of the smaller corner vortex. In all cases discussed, for $\mathcal{H} = 1$ (2D flow), we are able to identify smaller corner (Moffat) vortices downstream of the expansion plane in addition to the primary vortices, as shown by the inset in Figure 12e.

5. Velocity Field in the Contraction-Expansion

The velocity field was determined experimentally using μPIV as described in Section 2.2 and compared to the numerical calculations. To assess the evolution of the velocity along the lateral direction as the contraction is approached, we have plotted both experimental and numerical velocity profiles for the center plane ($y = 0$) and for various axial positions upstream of the contraction (-298 μm $\leq z \leq$ -47 μm). In Figure 14a, we depict the transverse profiles of the axial velocity V_z and in Figure 14b of the lateral velocity V_x, both normalized with the average axial velocity upstream of the contraction. For an axial position well upstream the contraction plane (z = -298 μm), the profiles approach those of fully-developed flow in a channel of rectangular cross-section. As we move towards the contraction plane, the streamlines converge towards the centerline. This causes the axial velocity near the walls $\left(0.4 \lesssim \left|x/(w_u/2)\right| \lesssim 1\right)$ to decrease, while the lateral velocity increases substantially relative to the fully-developed flow. The maximum velocity attained at the centerline ($y = 0$, $x = 0$) increases as we approach $z = 0$ and the effects of the contraction become more noticeable.

The experimental and predicted axial velocity profiles along the centerline upstream of the contraction are shown in Figure 15 for Q = 1 ml/h (Re = 7.3). The axial velocity is scaled with the average upstream velocity and is compared to the equivalent numerical calculations. The profile evolves from fully developed in the upstream part of the channel far away from the contraction (where the centerline velocity is constant) to a region $(-5 \lesssim z/w_c \lesssim 0)$ where the fluid accelerates as the contraction plane is approached. The numerical simulation is able to capture with good accuracy both the point at which the velocity starts to increase in the experiment, as well as the rate of increase. To provide a global comparison of the numerical computations and experimental measurements, we show contour plots of the velocity field upstream of the contraction in Figure 16. Again, good agreement is obtained between numerical simulations and experimental results.

In Figure 17a, we extend Figure 15 (for AR = 2.12) to show the computed axial velocity profiles over a larger range of axial positions along the centerline (including the upstream channel, the contraction and the downstream channel) and for a broader range of flow rates (0.1 ml/h $\leq Q \leq$ 6ml/h). Figure 17b shows the corresponding strain rate profile ($\partial V_z/\partial z$) along the centerline. The expected symmetrical behavior of the velocity profile, characteristic of

creeping flows, can be readily observed for the lower flow rates. For the lowest flow rate, $Q = 0.1$ ml/h ($Re = 0.73$), the velocity and velocity gradient profiles are symmetric. Consequently, just by looking at streak patterns or streamlines (Figure 18a) we would not be able to identify which direction the fluid is flowing, since at this low Reynolds number the flow is reversible (Acheson 1990) and the streamlines upstream and downstream of the contraction are coincident. In this case, due to the small depth of the geometry ($AR = 2.12$), the flow in the z-x plane approaches a potential flow and is very similar to that observed in a Hele-Shaw apparatus, as illustrated in Figure 18d. In Figure 18b, we superimpose computed streamlines and isobars (which coincide with the iso-lines of velocity potential in a 2D potential flow) in such a way that it resembles the flow net for a potential flow. Also of interest is the absence of the Moffat corner vortex characteristic of 2D viscous corner flows (Moffat 1964). This vortex is present even under inertialess flow conditions in simulations of 2D flows and in general for high aspect ratios ($AR >> 1$).

For higher flow rates, the profiles shown in Figure 17 are no longer symmetric about the line $z = L_c / 2$, and it takes longer for the velocity to decay towards its fully-developed state. In addition, for most of these flow rates, the flow does not have a long enough residence time to fully develop in the contraction throat (see inset in Figure 17a). Therefore, the results downstream of the contraction cannot be directly compared to those obtained in a simple expansion geometry, where fully-developed flow in the upstream channel is usually imposed as an inlet condition (see e.g. Drikakis 1997). In our case, the maximum velocity at the contraction exit is, in most cases, below the actual fully-developed value. As the flow rate increases, steady symmetric vortices grow downstream of the expansion plane. This, results in slower deceleration of material elements and a marked reduction in the extension rate $\partial V_z/\partial z$ downstream of the expansion plane. By contrast the upstream profile remains almost unchanged with changes in flow rate and a maximum value given by $(\partial V_z/\partial z)_{max} \approx 0.8 \langle v_z \rangle_c / w_c$. This is an important result from a rheometric point of view; it allows the control of the (dimensional) strain rate by controlling the flow rate and then measuring the resulting pressure drop.

6. Pressure Drop

The global pressure drop ΔP_{12} between the two pressure taps (located 3 mm upstream and downstream of the contraction plane) was measured experimentally using differential pressure

sensors as discussed in Section 2.3. In Figure 19 we compare experimental data for the global pressure drop with the corresponding numerical predictions. We examine the effect of inertia, by varying the flow rate in the range $Q \leq 12$ ml/h (substituting for the relevant geometric quantities and the properties of water we find $Re = 7.28\,Q$, with Q in ml/h). The geometry, with $L_c = 100$ μm and $h = 55$μm, was chosen to match the experimental conditions of Rodd et al. (2005). For low flow rates ($Q \leq 2$ ml/h), and therefore low Reynolds numbers, the pressure drop is seen to increase linearly with Q as expected. As the flow rate is further increased the nonlinear convective terms in the momentum equation become important and the total pressure drop starts to deviate from the linear viscous scaling, as can be clearly observed in the *log-log* inset on Figure 19. Close agreement is observed between the numerical and experimental results over the whole range of experimental conditions.

Experimentally, it is a challenging task to obtain further details regarding the local evolution of the pressure field within the channel. Numerically, however, we can probe the pressure field in detail. In Figures 20a and b, we show the evolution of the dimensionless pressure along the centerline ($y = 0$ and $x = 0$) to illustrate the effect of flow rate and contraction length on the pressure profiles, respectively. In Figure 20a, we also show for reference the scaled pressure expected for a hypothetical fully-developed flow in all channels. This serves as a useful reference for comparisons. The effect of the contraction is clear, and is manifested in a drop in pressure just upstream of the entrance to the throat. This pressure drop is associated with the flow rearrangement near the contraction plane and is the main source of the difference between the computed profile and the hypothetical locally fully-developed flow. There is also a small, but noticeable, exit effect near the expansion plane. The viscous flow in the narrow channel develops very rapidly at these flow rates. Varying the total length of the channel as shown in Figure 20b changes the total pressure drop across the device but does not influence the entrance correction appreciably.

Figure 21 shows the longitudinal pressure gradient $\partial p/\partial z$ along the centerline for the contraction-expansion for a range of flow rates ($0.1\text{ml/h} \leq Q \leq 6$ ml/h). There is an initial region of abrupt increase in the pressure gradient, from a situation of fully-developed flow away from the contraction to a maximum at the contraction plane. As the flow rate and Reynolds number increase, the increase in the normalized pressure gradient becomes more pronounced. For the lowest flow rate, due to reversibility of creeping flow, the exit region is a mirror image of the entrance region and the maximum pressure gradient attained corresponds

to that of a fully-developed flow in the narrow channel. For higher flow rates, the pressure gradient beyond the contraction plane decays until it reaches a constant value consistent with Poiseuille flow in a channel of width w_c and depth h. Just upstream of the expansion plane, the pressure gradient starts to decrease once more, until it eventually becomes constant far downstream from the expansion at the value expected for viscous flow in a channel that is approximately 16 times wider than the throat. For the two highest flow rates, the pressure gradient actually changes sign before reaching this constant value as a result of the recirculating vortices downstream of the expansion plane. To summarize these observations, the contraction entrance region is responsible for a large fraction of the extra pressure drop, and this increases substantially with inertia.

We now proceed to focus on the extra (or excess) pressure drop Δp_{exc} associated with the contraction-expansion flow. This cannot be readily measured in experiments but can be evaluated from measurements of the total pressure drop and application of an appropriate analytic decomposition (Boger 1987; Kang et al. 2006). Numerical computations of the full pressure field can be used to explore the validity of the protocols employed in processing the experimental data.

The excess pressure drop is calculated by subtracting from the global pressure drop the net pressure drop associated with the fully-developed Poiseuille flow in the upstream and downstream parts of the channel, plus that in the narrow contraction:

$$\Delta p_{\mathrm{exc}} = \Delta p_{12} - \left(\frac{\mathrm{d}p}{\mathrm{d}z}\right)_{\mathrm{u}} L_{\mathrm{u}} - \left(\frac{\mathrm{d}p}{\mathrm{d}z}\right)_{\mathrm{d}} L_{\mathrm{d}} - \left(\frac{\mathrm{d}p}{\mathrm{d}z}\right)_{\mathrm{c}} L_{\mathrm{c}} \qquad (7)$$

where the subscript ‘u’ refers to the channel upstream of the contraction plane, ‘d’ to the channel downstream of the expansion plane, and ‘c’ to the narrow channel in the contraction region.

An alternative dimensionless quantity commonly reported is the Couette correction C (Boger 1982), defined as the excess pressure drop arising from the sudden contraction and expansion scaled with $2\tau_w$, where τ_w is the average wall shear stress in the fully-developed flow in the contraction channel:

$$2\tau_w = -(\mathrm{d}p/\mathrm{d}z)_c \; D_{h,c} / 2 \qquad (8)$$

The effect of inertia ($Q \leq 12$ ml/h; $Re \leq 87.4$) on the excess pressure drop and corresponding Couette correction are presented in Figure 22. The excess pressure drop arises mainly from the entrance effects described in our analysis of Figure 20. These entry effects become more pronounced at higher flow rates, and thus the excess pressure drop and Couette correction increase substantially with Re. For the range of contraction lengths tested, L_c does not seem to have an effect on the excess pressure drop, provided that the pressure gradient has enough space to fully develop and that there are portions of the narrow contraction where the entrance and exit effects are not felt. This is achieved for the range of flow rates used, except for the case of the contraction with length $L_c = 100$ μm and for the higher flow rates, $Q \geq 8$ ml/h ($Re \geq 58.3$).

The Bagley analysis and associated Bagley plot is a common tool in the polymer processing field in which axisymmetric capillaries are generally used to measure entrance effects in complex fluids (Kim and Dealy 2001). The Bagley plot is a graph of the total pressure drop versus the length to diameter ratio of the die, with apparent wall shear rate as the control parameter (Kim and Dealy 2001). The measured data falls on straight lines each corresponding to a specific value of the apparent shear rate and extrapolation to the limit of zero capillary length gives the excess pressure drop. Typically for axisymmetric geometries, the total pressure drop is calculated between two points, one at a fixed upstream location ($z = -z_0$) and the other on the free jet exiting downstream (atmospheric pressure), for several different L_c keeping the flow rate constant. The extrapolation of the fitted straight line to $L_c = 0$ allows the calculation of the Bagley excess pressure drop and corresponding dimensionless Bagley correction (Mitsoulis et al. 1998). This method yields good results in axisymmetric contractions with high contraction ratios, since the pressure drop upstream of the contraction due to fully-developed flow as well as at the exit of the capillary are negligible compared to the excess pressure drop. In the case of microfluidic devices, where the channels are typically planar with a constant out-of-plane dimension (i.e. depth) smaller than the upstream channel width, the effective contraction ratio – based on hydraulic diameters ($D_{h,u}/D_{h,c}$) – is much smaller when compared at an equivalent nominal contraction ratio w_u/w_c as in the axisymmetric case. In such cases, depending on the positions z_0 chosen for the pressure transducers we would obtain different values of ΔP_{exc}. It is thus helpful to rethink the Bagley analysis for microfluidic devices. To determine the equivalent to the Bagley correction

for such planar geometries, the total pressure drop was calculated between pressure taps located at positions that are proportional to the length of the contraction. For example, the total pressure drop for the Bagley plot, $\Delta P_{\text{Bagley,}}$ for the contraction-expansion device should be calculated between:

- $z = -\alpha$ and $z = L_c + \beta$, for $L_c = 100$ μm,
- $z = -2\alpha$ and $z = L_c + 2\beta$, for $L_c = 200$ μm,
- $z = -4\alpha$ and $z = L_c + 4\beta$, for $L_c = 400$ μm.

for the contraction-expansions simulated in the present work, i.e. $L_c = 100$, 200 and 400 μm. Extrapolation to the limiting case $L_c = 0$ of the straight line fitted to the total pressure drop will yield the relevant Bagley correction. Using this construction, the calculated ΔP_{exc} will be the same, whatever α and β values we decide to use, provided that they are proportional to the contraction length and that they are sufficiently separated from the contraction so that there are no exit or entrance effects. In the calculations, we have used arbitrarily the values $\alpha = \beta = 1$ mm.

Figure 23 shows the Bagley plot corresponding to our contraction-expansion geometry for various Reynolds numbers in the range from $Re = 0$ (creeping flow) to $Re = 87.4$. We used three different lengths of the contraction: 100, 200 and 400 μm, and since we are dealing with a planar geometry, we report the ratio of L_c to the width of the contraction channel, w_c. As expected, for the lower flow rates, the total pressure drop increases linearly as a function of the length of the contraction. For the two highest flow rates there is a very slight deviation from linearity, which is related to the fact that for the shorter contraction the residence time of material elements in the narrow channel is not sufficient for the flow to develop fully. This will have an effect on the accuracy of the Bagley prediction of excess pressure drop. The Bagley analysis results in the same values as the corresponding Couette correction, except for the highest Reynolds numbers ($Re > 50$), for which the Bagley analysis yields slightly lower values. If we calculate the Bagley correction for the highest Reynolds numbers ($Re = 58.3$ and $Re = 87.4$) using only on the data corresponding to $L_c = 200$ and 400 μm (where the flow is fully developed in the middle of the smaller channel), then we achieve perfect agreement between both methods. This is an important finding, since the Bagley method of determining the excess pressure drop is likely to be more amenable for use in an experimental context.

It is clear from Figure 22 that the dimensionless excess pressure drop varies with the Reynolds number in a non-linear fashion, in contrast with the findings of Kang et al. (2006),

who reported that $\Delta P_{exc}/2\tau_w$ varies linearly with *Re* (or *Q*). A possible explanation might be related to the geometrical configuration: Kang et al. (2006) use a geometry with a contraction only while we use a contraction followed by an expansion. In their work, the average velocity in the larger channel (where the first pressure tap is located) is much smaller that that in the contraction (where the second pressure tap is located) and therefore there is a difference in the kinetic energy of the fluid at each pressure tap location. This is in agreement with the analysis of Boger (1982) who reports:

$$\frac{\Delta P_{exc}}{2\tau_w} = (B+1)\frac{Re}{32} + C \tag{9}$$

where *B* is a parameter that arises from the boundary layer development and *C* is the inertialess Couette correction term coming from the flow profile change at the entry plane. For an axisymmetric contraction $B = 0.0709$ and $C = 0.589$ (Boger 1982). The dimensionless pressure drop arising from this difference in upstream and downstream kinetic energies is linear (when scaled with a viscous stress) and dominates over the other terms for moderate *Re*. In the case of a contraction-expansion configuration, there is no velocity difference between the two pressure taps, and linearity is not necessarily expected. We have also analyzed the relationship between $\Delta P_{exc}/2\tau_w$ and the Reynolds number for our geometry by considering a second pressure tap located in the contraction region rather than downstream of the expansion. In this case, $\Delta P_{exc}/2\tau_w$ is indeed a linear function of *Re* in accordance with the findings of Boger (1982) and Kang et al. (2006).

As in the previous section, we have also studied the effect of the aspect ratio *AR* on the pressure drop for a range of Reynolds number, and this is shown in Figure 24. The Couette correction, calculated using Eqs. (7) and (8), increases with the Reynolds number for high values of *h*, but approaches a constant value independent of *Re* as the channel depth decreases; however, this value depends on *h* itself. Better insight is obtained if instead we plot a modified Couette correction, *C**, defined as $C^* = \frac{\Delta P_{exc}}{2\tau_w^*} = \frac{\Delta P_{exc}}{-(dp/dz)_{\text{contraction}} \times w_c}$, as a function of the Re_{w_c}, as defined in Eq. (6). This parameter represents the extra pressure drop due to the contraction-expansion in terms of the number of equivalent multiples of the (small) microchannel widths that would produce the same pressure loss. The meaning of this parameter can be more easily understood by analogy with the pressure drops reported in

turbulent flows that arise from minor losses in pipe systems. These are commonly expressed as a loss factor K which can also be related to the number of equivalent pipe diameters. The asymptotic behavior of the excess pressure drop is now much clearer: the modified Couette correction is bounded between two limiting cases corresponding to Hele-Shaw flow and 2D flow. For low Re_{w_c}, the results are bounded between 0.84 (2D flow, $AR \to \infty$) and 1.52 (Hele-Shaw flow, $AR \to 0$). For high aspect ratios, the modified Couette correction increases substantially with increasing inertia beyond $Re_{w_c} \approx 5$, as illustrated in Figure 24b.

7. Conclusions

A series of numerical simulations have been performed for Newtonian fluid flow through an abrupt contraction-expansion microfluidic device over a range of aspect ratios and Reynolds numbers. The numerical results are in good agreement with experimental measurements of the kinematics and pressure drop for the same conditions (fluid and geometry). The numerical calculations allow for a more detailed analysis of the flow and a broader range of conditions than the experiments, thus complementing the experimental work and guiding future device design.

It was shown that although the flow may appear to be quasi-two-dimensional, in fact, for typical values of the aspect ratio that can be obtained experimentally, it is highly three-dimensional with open spiraling vortical structures in the stagnant corner regions. For the range of Re values which can be achieved experimentally in our set-up ($Re \lesssim 90$, $AR = 2.1$), computations and observation show that the flow always remains symmetric about the center plane. As the flow rate is increased, and inertial effects become important, the formation and growth of lip vortices is observed downstream of the expansion. At $Re \approx 20$, the lip vortices reach the outer walls of the expansion geometry and grow downstream. Beyond this transition, the vortex size increases monotonically with Re. Two-dimensional simulations were also carried out in a corresponding idealized channel (corresponding to $AR >> 1$) in which the effects of the upper and lower endwalls are negligible. A supercritical bifurcation is found in 2D flow for a critical Reynolds number of $Re_{(2D)_c} \approx 28$. The flow asymmetries become more pronounced with increasing Reynolds number, and large stable recirculations are formed downstream of the expansion. This work illustrates that even relatively simple planar contraction-expansion geometries can lead to highly complex and three-dimensional

flows. Simpler 2D approximations may lead to large quantitative errors in their predictions which may not even be qualitatively acceptable.

The dimensionless excess pressure drop associated with the converging-diverging flow was evaluated using both the Couette and Bagley approaches. We suggest a modified means of calculating the Bagley correction which appears to be more appropriate for planar microchannels with a contraction followed by an expansion. In this way, the Couette and Bagley correction methods yield consistent results provided fully-developed flow is attained at some point in the contraction region. The excess pressure drop is caused primarily by the flow rearrangement in the entrance region, which becomes more pronounced as the Reynolds number is increased. The effect of varying the device aspect ratio (AR) on the excess pressure drop has also been studied in detail. Analysis of both the computed velocity and pressure fields show that the results are bound between two well-defined limiting cases: that of 2D viscous flow ($AR \rightarrow \infty$) and viscous potential flow in the limiting case of Hele-Shaw flow ($AR \rightarrow 0$).

The ability of the three-dimensional numerical calculations to accurately capture both the kinematics and dynamics observed experimentally provides a mechanism for rapidly exploring the consequences of changes to the geometric parameters governing the flow in a microfluidic device. This computational rheometric capability will prove useful in optimizing the design of future microfluidic rheometers.

References

Acheson DJ (1990) Elementary Fluid Dynamics. Oxford University Press, Oxford

Alves MA, Pinho FT, Oliveira PJ (2000) Effect of a high-resolution differencing scheme on finite-volume predictions of viscoelastic flows. Journal of Non-Newtonian Fluid Mechanics 93:287-314

Alves MA, Oliveira PJ, Pinho FT (2003) A Convergent and Universally Bounded Interpolation Scheme for the Treatment of Advection. International Journal for Numerical Methods in Fluids 41:47-75

Alves MA, Oliveira PJ, Pinho FT (2004) On the Effect of Contraction Ratio in Viscoelastic Flow through Abrupt Contractions. Journal of Non-Newtonian Fluid Mechanics 122:117-130

Alves MA, Pinho FT, Oliveira PJ (2005) Visualizations of Boger Fluid Flows in a 4 : 1 Square-Square Contraction. AIChE Journal 51:2908-2922

Bagley EB (1957) End Corrections in the Capillary flow of polyethylene (1957) Journal of Applied Physics 28:624-627

Barnes HA, Hutton JF, Walters K (1989) An Introduction to Rheology. Elsevier : Distributors for the U.S. and Canada, Elsevier Science Pub. Co., Amsterdam ; New York

Barrat JL, Bocquet L (1999) Large Slip Effect at a Nonwetting Fluid-Solid Interface. Physical Review Letters 82:4671-4674

Battaglia F, Tavener SJ, Kulkarni AK, Merkle CL (1997) Bifurcation of Low Reynolds Number Flows in Symmetric Channels. AIAA Journal 35:99-105

Bayraktar T, Pidugu SB (2006) Characterization of Liquid Flows in Microfluidic Systems. International Journal of Heat and Mass Transfer 49:815-824

Binding DM (1988) An Approximate Analysis for Contraction and Converging Flows. Journal of Non-Newtonian Fluid Mechanics 27:173-189

Binding DM, Couch MA, Walters K (1998) The Pressure Dependence of the Shear and Elongational Properties of Polymer Melts. Journal of Non-Newtonian Fluid Mechanics 79:137-155

Binding DM, Phillips PM, Phillips TN (2006) Contraction/expansion flows: The pressure drop and related issues. Journal of Non-Newtonian Fluid Mechanics 137:31-38

Boger DV (1982) Circular Entry Flows of Inelastic and Viscoelastic Fluids. In Advances of Transport Processes, AS Mujumdar, RA Mashelkar (eds.) 2:43-98

Boger DV (1987) Viscoelastic Flows through Contractions. Annual Review of Fluid Mechanics 19:157-182

Boger DV, Binnington RJ (1990) Circular Entry Flows of Fluid M1. Journal of Non-Newtonian Fluid Mechanics 35:339-360

Brown RA, McKinley GH (1994) Report on the VIIIth Int Workshop on Numerical-Methods in Viscoelastic Flows. Journal of Non-Newtonian Fluid Mechanics 52:407-413

Cherdron W, Durst F, Whitelaw JH (1978) Asymmetric Flows and Instabilities in Symmetric Ducts with Sudden Expansions. Journal of Fluid Mechanics 84:13-31

Chiang TP, Sheu TWH, Wang SK (2000) Side Wall Effects on the Structure of Laminar Flow over a Plane-Symmetric Sudden Expansion. Computers & Fluids 29:467-492

Chow AW (2002) Lab-on-a-chip: Opportunities for chemical engineering. AIChE Journal 48:1590-1595

Cogswell FN (1972a) Converging Flow of Polymer Melts in Extrusion Dies. Polymer Engineering and Science 12:64-73

Cogswell FN (1972b) Measuring Extensional Rheology of Polymer Melts. Transactions of the Society of Rheology 16:383-403

Drikakis D (1997) Bifurcation Phenomena in Incompressible Sudden Expansion Flows. Physics of Fluids 9:76-87

Durst F, Melling A, Whitelaw JH (1974) Low Reynolds-Number Flow over a Plane Symmetric Sudden Expansion. Journal of Fluid Mechanics 64:111-128

Durst F, Pereira JCF, Tropea C (1993) The Plane Symmetrical Sudden-Expansion Flow at Low Reynolds-Numbers. Journal of Fluid Mechanics 248:567-581

Fearn RM, Mullin T, Cliffe KA (1990) Nonlinear Flow Phenomena in a Symmetric Sudden Expansion. Journal of Fluid Mechanics 211:595-608

Gad-el-Hak M (2002) The MEMS Handbook. CRC Press, Boca Raton, FL

Hassager O (1988) Working Group on Numerical Techniques (Vth Workshop on Numerical Methods in Non-Newtonian Flow). Journal of Non-Newtonian Fluid Mechanics 29:2-5

Hawa T, Rusak Z (2001) The Dynamics of a Laminar Flow in a Symmetric Channel with a Sudden Expansion. Journal of Fluid Mechanics 436:283-320

James DF, Chandler GM, Armour SJ (1990) A Converging Channel Rheometer for the Measurement of Extensional Viscosity. Journal of Non-Newtonian Fluid Mechanics 35:421-443

Kang K, Lee LJ, Koelling KW (2005) High Shear Microfluidics and its Application in Rheological Measurement. Experiments in Fluids 38: 222-232

Kang K, Koelling KW, Lee LJ (2006) Microdevice End Pressure Evaluations with Bagley Correction. Microfluidics and Nanofluidics 2:223-235

Karniadakis G, Beskok A, Aluru NR (2005) Microflows and Nanoflows : Fundamentals and Simulation. Springer Verlag, New York, NY

Kim S, Dealy JM (2001) Design of an Orifice Die to Measure Entrance Pressure Drop. Journal of Rheology 45:1413-1419

Koo JM, Kleinstreuer C (2003) Liquid Flow in Microchannels: Experimental Observations and Computational Analyses of Microfluidics Effects. Journal of Micromechanics and Microengineering 13:568-579-

Lauga E, Stroock AD, Stone HA (2004) Three-dimensional flows in slowly varying planar geometries. Physics of Fluids 16:3051–3062

Lee WY, Wong M, Zohar Y (2002a) Microchannels in Series Connected Via a Contraction/Expansion Section. Journal of Fluid Mechanics 459:187-206

Lee WY, Wong M, Zohar Y (2002b) Pressure Loss in Constriction Microchannels. Journal of Microelectromechanical Systems 11:236-244

Leonard BP (1979) Stable and Accurate Convective Modeling Procedure Based on Quadratic Upstream Interpolation. Computer Methods in Applied Mechanics and Engineering 19:59-98

McDonald JC, Duffy DC, Anderson JR, Chiu DT, Wu HK, Schueller OJA, Whitesides GM (2000) Fabrication of Microfluidic Systems in Poly(Dimethylsiloxane). Electrophoresis 21:27-40

Mishra S, Jayaraman K (2002) Asymmetric Flows in Planar Symmetric Channels with Large Expansion Ratio. International Journal for Numerical Methods in Fluids 38:945-962

Mitsoulis E, Hatzikiriakos SG, Christodoulou K, Vlassopoulos D (1998) Sensitivity Analysis of the Bagley Correction to Shear and Extensional Rheology. Rheologica Acta 37:438-448

Moffat HK (1964) Viscous and Resistive Eddies near a Sharp Corner. Journal of Fluid Mechanics 18:1-18

Neto C, Evans DR, Bonaccurso E, Butt HJ, Craig VSJ (2005) Boundary Slip in Newtonian Liquids: A Review of Experimental Studies. Reports on Progress in Physics 68:2859-2897

Ng JMK, Gitlin I, Stroock AD, Whitesides GM (2002) Components for Integrated Poly(Dimethylsiloxane) Microfluidic Systems. Electrophoresis 23:3461-3473

Nguyen NT, Wu ZG (2005) Micromixers - a Review. Journal of Micromechanics and Microengineering 15:R1-R16

Oliveira MSN, Alves MA, McKinley GH, Pinho FT (2007a) Viscous Flow through Microfabricated Hyperbolic Contractions. Experiments in Fluids DOI: 10.1007/s00348-007-0306-2

Oliveira MSN, Oliveira PJ, Pinho FT, Alves MA (2007b) Effect of Contraction Ratio upon Viscoelastic Flow in Contractions: The Axisymmetric Case. *Submitted to* Journal of Non-Newtonian Fluid Mechanics

Oliveira MSN, Yeh R, McKinley GH (2006) Iterated Stretching, Extensional Rheology and Formation of Beads-on-a-String Structures in Polymer Solutions. Journal of Non-Newtonian Fluid Mechanics 137:137-148

Oliveira PJ (2003) Asymmetric Flows of Viscoelastic Fluids in Symmetric Planar Expansion Geometries. Journal of Non-Newtonian Fluid Mechanics 114:33-63

Oliveira PJ, Pinho FT (1999) Numerical Procedure for the Computation of Fluid Flow with Arbitrary Stress-Strain Relationships. Numerical Heat Transfer Part B-Fundamentals 35:295-315

Oliveira PJ, Pinho FT, Pinto GA (1998) Numerical Simulation of Non-Linear Elastic Flows with a General Collocated Finite-Volume Method. Journal of Non-Newtonian Fluid Mechanics 79:1-43

Owens RG, Phillips NT (2002) Computational Rheology. Imperial College Press, London

Pit R, Hervet H, Leger L (2000) Direct Experimental Evidence of Slip in Hexadecane: Solid Interfaces. Physical Review Letters 85:980-983

Poole RJ, Alves MA, Oliveira PJ, Pinho FT (2007) Plane Sudden Expansion Flows of Viscoelastic Liquids. Journal of Non-Newtonian Fluid Mechanics (*In Press*) DOI: 10.1016/j.jnnfm.2006.11.001

Revuelta A (2005) On the Two-Dimensional Flow in a Sudden Expansion with Large Expansion Ratios. Physics of Fluids 17:028102 1-4

Rodd LE, Scott TP, Boger DV, Cooper-White JJ, McKinley GH (2005) The Inertio-Elastic Planar Entry Flow of Low-Viscosity Elastic Fluids in Micro-Fabricated Geometries. Journal of Non-Newtonian Fluid Mechanics 129:1-22

Rothstein JP, McKinley GH (2001) The Axisymmetric Contraction-Expansion: The Role of Extensional Rheology on Vortex Growth Dynamics and the Enhanced Pressure Drop. Journal of Non-Newtonian Fluid Mechanics 98:33-63

Scott TP (2004) Contraction/Expansion Flow of Dilute Elastic Solutions in Microchannels, M.S. thesis, Mechanical Engineering. MIT, Cambridge, MA

Shapira M, Degani D, Weihs D (1990) Stability and Existence of Multiple Solutions for Viscous-Flow in Suddenly Enlarged Channels. Computers & Fluids 18:239-258

Sharp KV, Adrian RJ (2004) Transition from Laminar to Turbulent Flow in Liquid Filled Microtubes. Experiments in Fluids 36:741-747

Sobey IJ, Drazin PG (1986) Bifurcations of Two-Dimensional Channel Flows. Journal of Fluid Mechanics 171:263-287

Stone HA, Stroock AD, Ajdari A (2004) Engineering Flows in Small Devices: Microfluidics toward a Lab-on-a-Chip. Annual Review of Fluid Mechanics 36:381-411

Townsend P, Walters K (1994) Expansion Flows of Non-Newtonian Liquids. Chemical Engineering Science 49:749-763

Tsai C-H, Chen H-T, Wang Y-N, Lin C-H, Fu L-M (2006) Capabilities and Limitations of 2-Dimensional and 3-Dimensional Numerical Methods in Modeling the Fluid Flow in Sudden Expansion Microchannels. Microfluidics and Nanofluidics DOI: 10.1007/s10404-006-0099-2

Tuladhar TR, Mackley MR (2007) Filament stretching rheometry and break-up behaviour of low viscosity polymer solutions and inkjet fluids. Journal of Non-Newtonian Fluid Mechanics DOI: 10.1016/j.jnnfm.2007.04.015

Wereley ST, Meinhart CD (2004) Micron-Resolution Particle Image Velocimetry. In: Breuer KS (ed) Microscale Diagnostic Techniques. Springer, Berlin, Heidelberg, New York

White SA, Gotsis AD, Baird DG (1987) Review of the Entry Flow Problem - Experimental and Numerical. Journal of Non-Newtonian Fluid Mechanics 24:121-160

Whitesides GM (2006) The Origins and the Future of Microfluidics. Nature 442:368-373

Whitesides GM, Stroock AD (2001) Flexible Methods for Microfluidics. Physics Today 54:42-48

Wille R, Fernholz H (1965) Report on First European Mechanics Colloquium on Coanda Effect. Journal of Fluid Mechanics 23:801-819

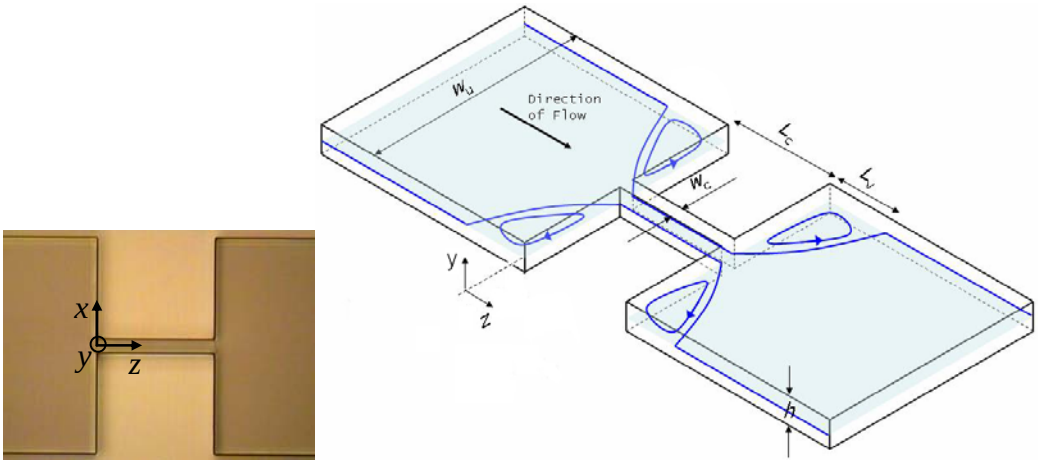

Figure 1. Optical transmission microscope image and schematic diagram of the 400:26:400 abrupt planar contraction-expansion showing the coordinate system and variables used throughout the text. The contraction ratio is defined as $CR = w_u/w_c$ and the aspect ratio as $AR = h/w_c$.

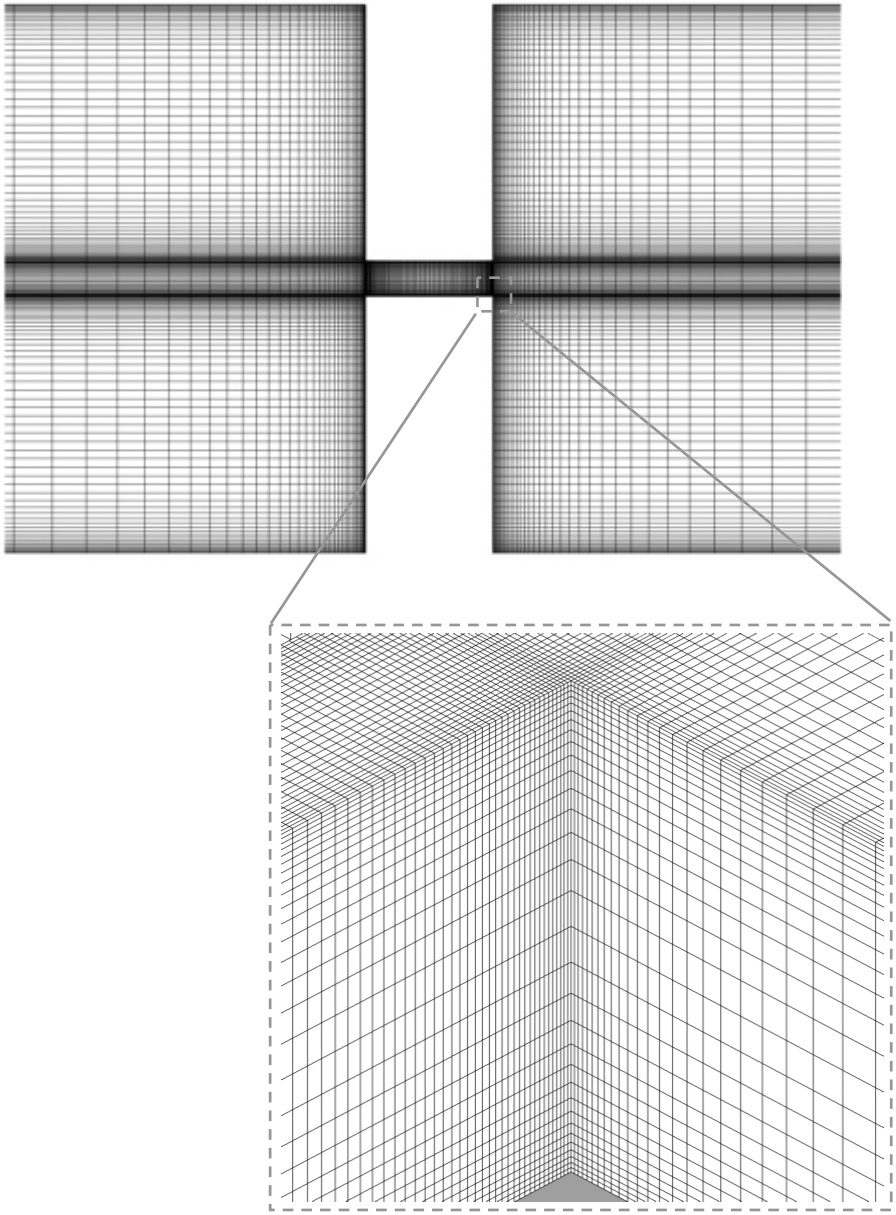

Figure 2. Zoomed view of mesh M2 near the contraction-expansion region showing details of the mesh near a sharp corner.

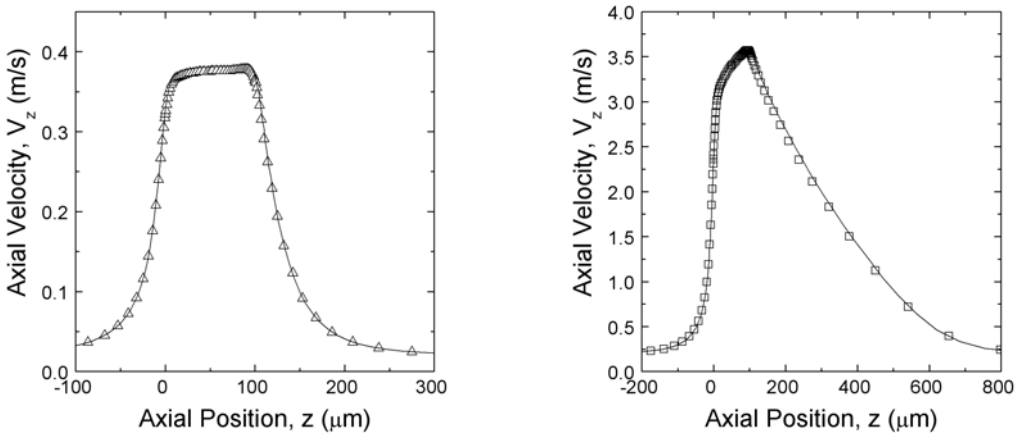

Q = 1 ml/h Q = 10 ml/h

(a)

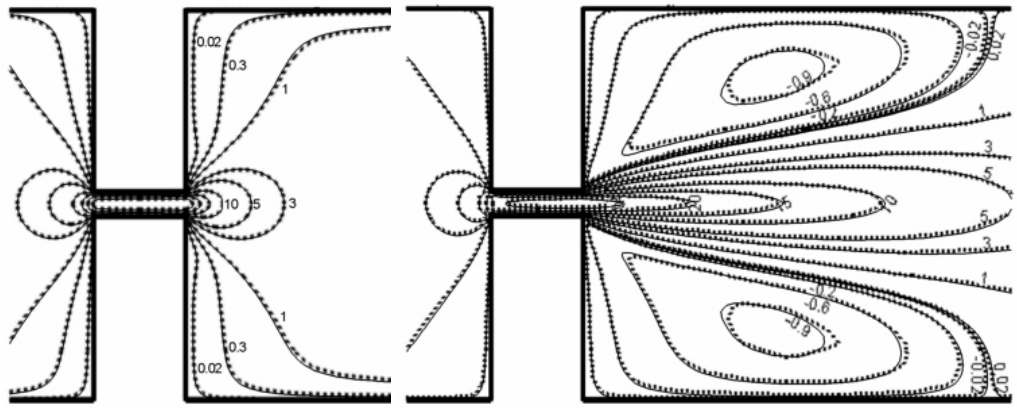

Q = 1 ml/h Q = 10 ml/h

(b)

Figure 3. Effect of mesh refinement on the velocity field for the 3D geometry (w_c = 26 μm, h = 55 μm, L_c = 100 μm): (a) Axial velocity profiles along the centerline (y = 0, x = 0) obtained numerically with the coarse mesh M1 (symbols) and the refined mesh M2 (line); (b) Normalized axial velocity ($V_z / < V_z >_u$) contour lines at the center plane (y = 0) upstream and downstream of the contraction obtained numerically with the coarse mesh M1 (dashed lines) and the refined mesh M2 (solid lines).

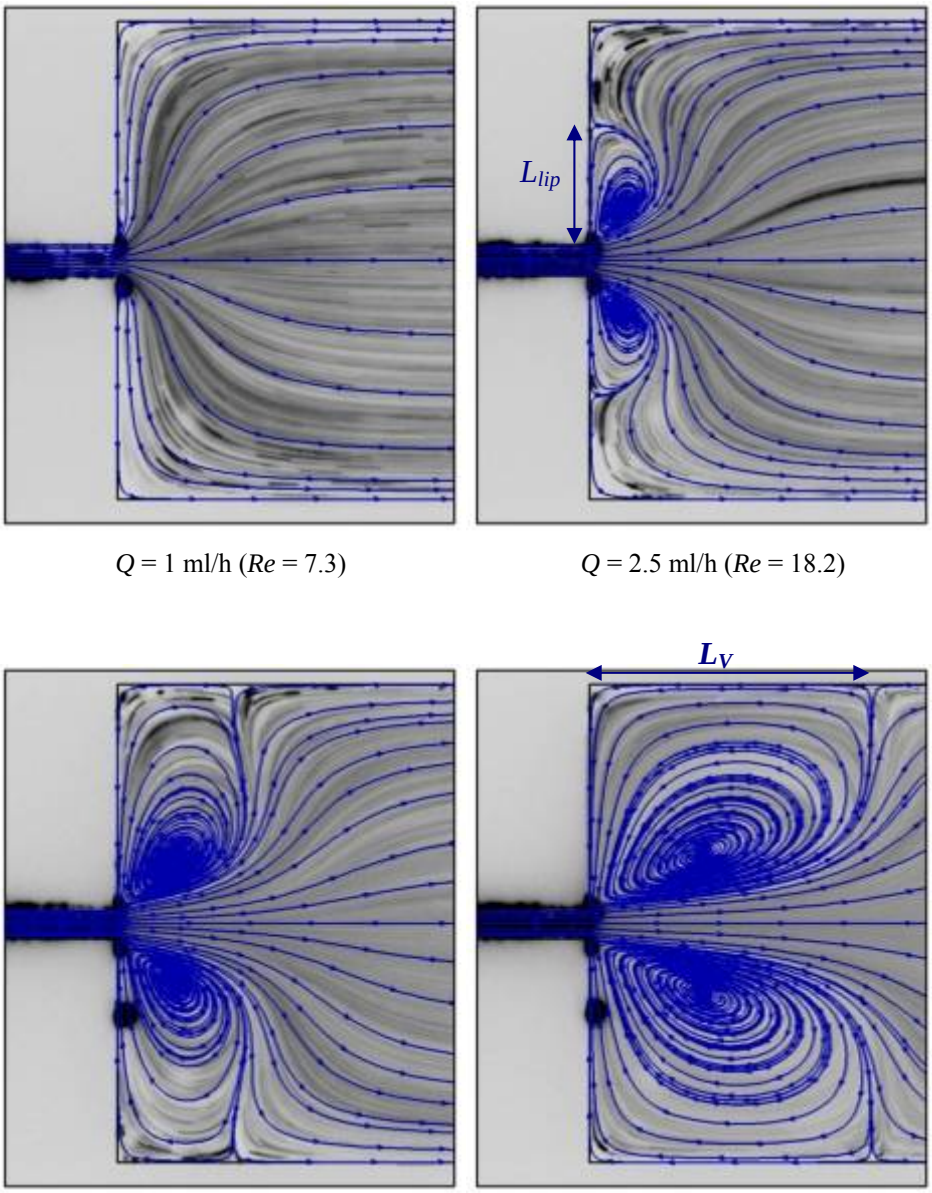

Figure 4. Effect of inertia on the experimental (photograph) and predicted streak lines (solid lines) obtained at the centre plane (y = 0) downstream of the contraction for water flowing through a 400:26:400 contraction-expansion with h = 55 μm and L_c = 200 μm.

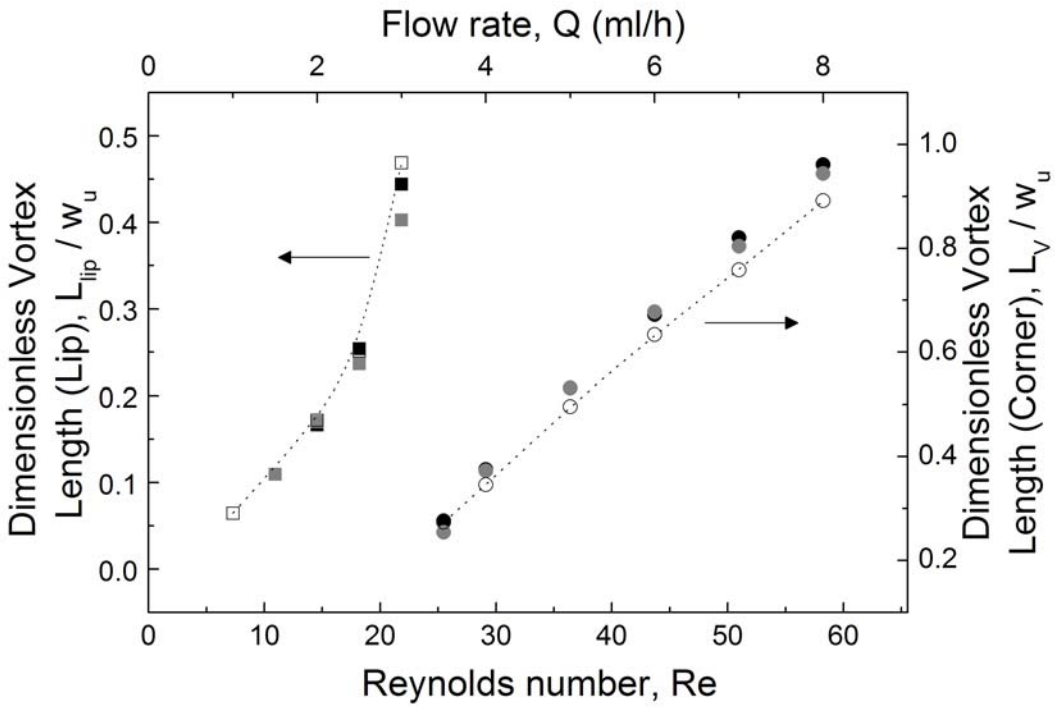

Figure 5. Effect of inertia on the dimensionless vortex length at the centre plane ($y = 0$) for the experimental geometry ($w_c = 26$ μm, $h = 55$ μm, $L_c = 200$ μm). The open symbols represent the numerical data; the dark and light filled symbols represent the experimental measurements of the upper and lower vortex sizes, respectively.

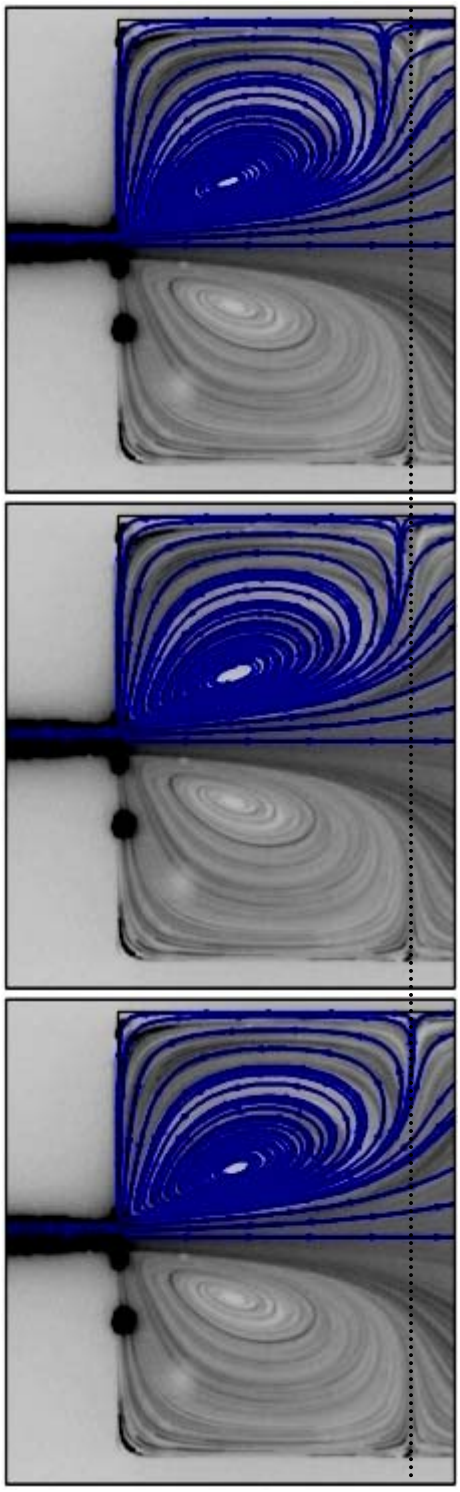

Figure 6. Experimental (photograph) and predicted streak lines (solid lines) at the centre plane ($y = 0$) downstream of the contraction ($w_c = 26$ μm, $L_c = 200$ μm) for a flow rate $Q = 6$ ml/h to highlight the sensitivity to imprecision of the measurement of the channel depth on the vortex size; $h = 50, 55, 60$ μm from top to bottom.

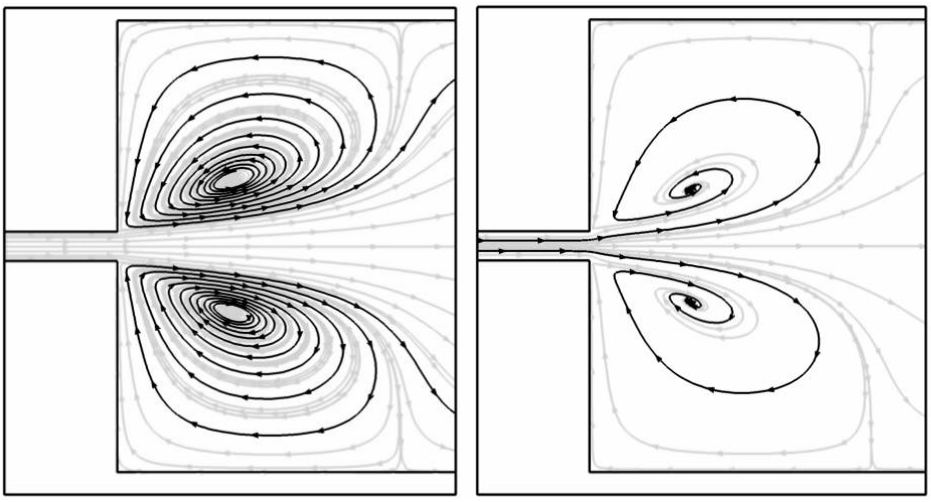

(a) (b)

Figure 7. Projected streamlines downstream of the contraction (w_c = 26 μm, h = 55 μm, L_c = 200 μm) for a flow rate Q = 6 ml/h (Re = 43.7) at (a) the centre plane (y = 0) and (b) near the wall $\left(y/(h/2)=0.98\right)$. In each image, one streamline is highlighted (in black) to show the distinct circulation patterns.

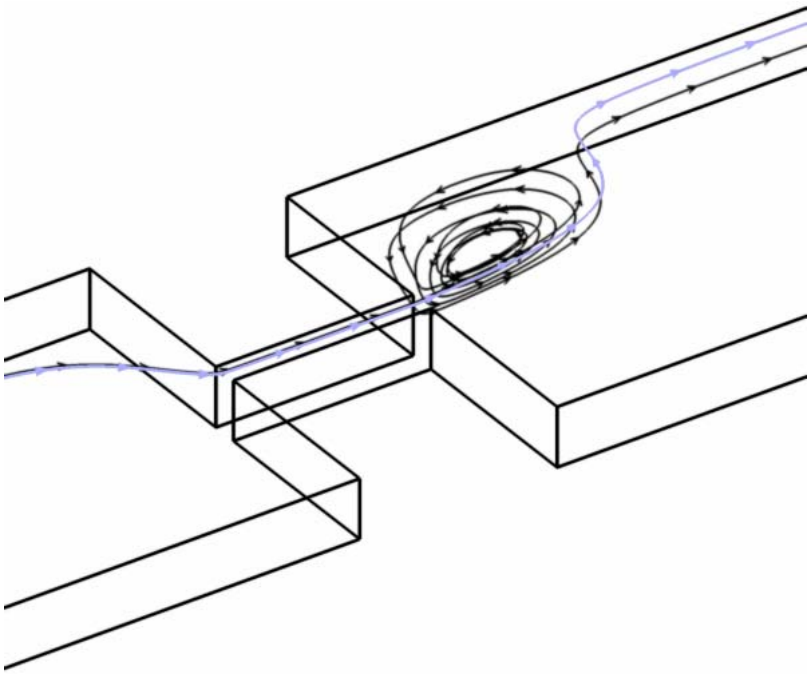

(a)

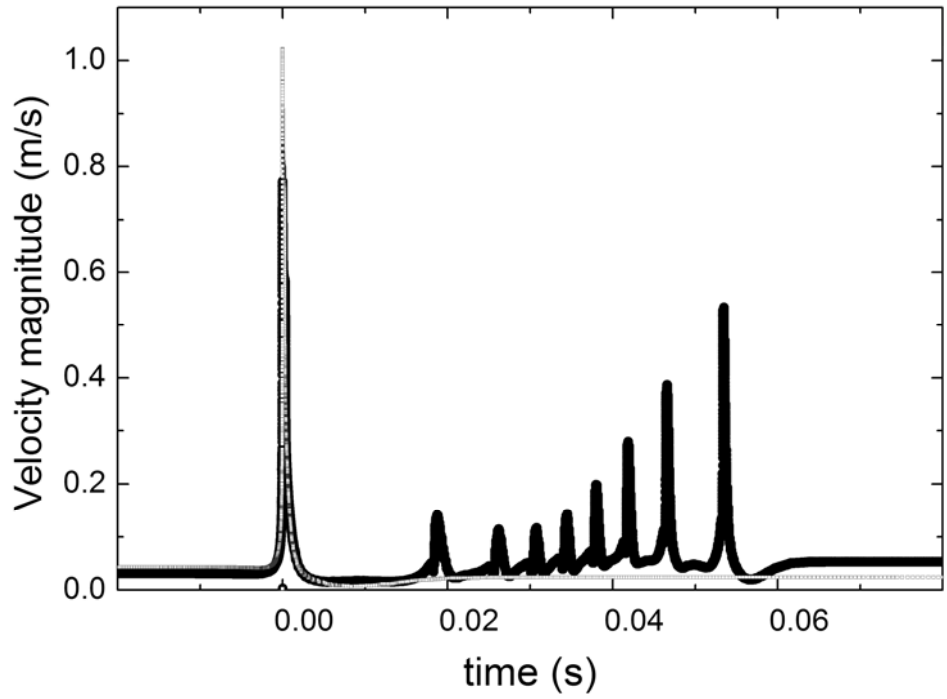

(b)

Figure 8. Trajectories (a) and time evolution of the velocity magnitude (b) of two material points through the sudden contraction-expansion (w_c = 26 μm; L_c = 200 μm; h = 55 μm), one that enters the recirculation (dark line) and goes through point z = 500 μm, x = 180 μm and y = 1 μm and another that does not enter the recirculation (light line) and goes through point z = 500 μm, x = 180 μm and y = 26.5 μm.

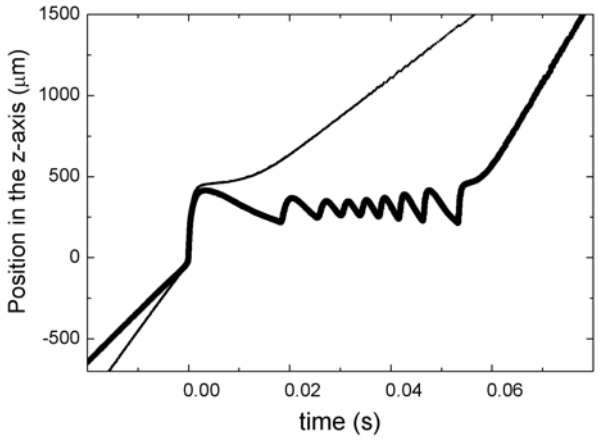

(a)

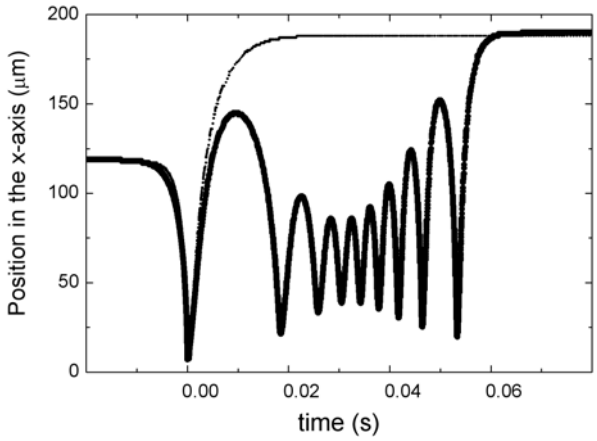

(b)

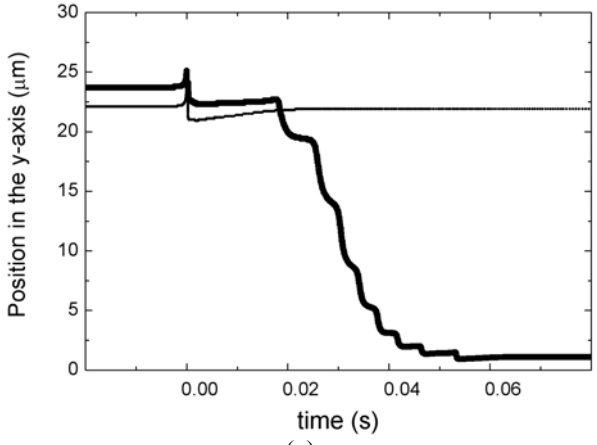

(c)

Figure 9. Lagrangian trajectories of the two material points illustrated in Figure 8.

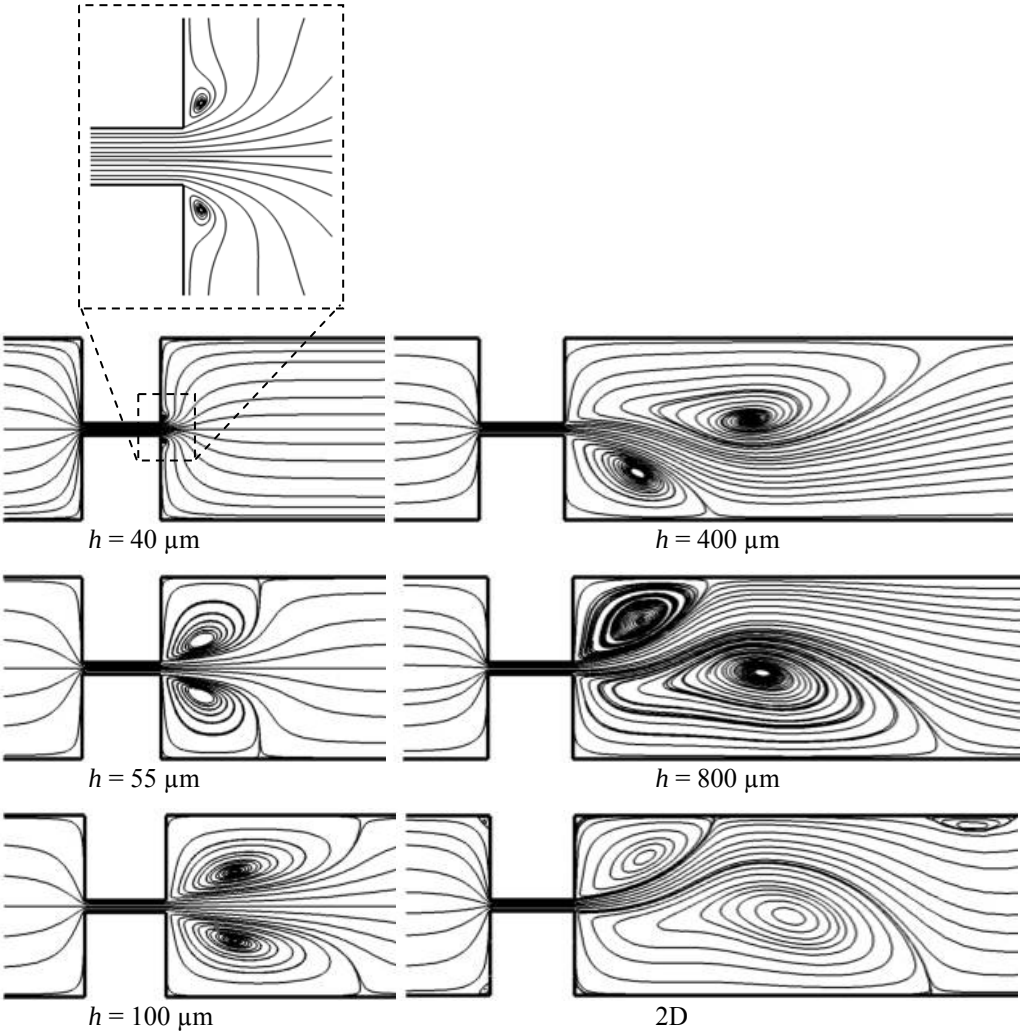

Figure 10. Effect of channel depth on the predicted streamlines at the center plane ($y = 0$) for a 400:26:400 contraction-expansion geometry with L_c = 200 μm, keeping the Reynolds number constant (Re = 43.7).

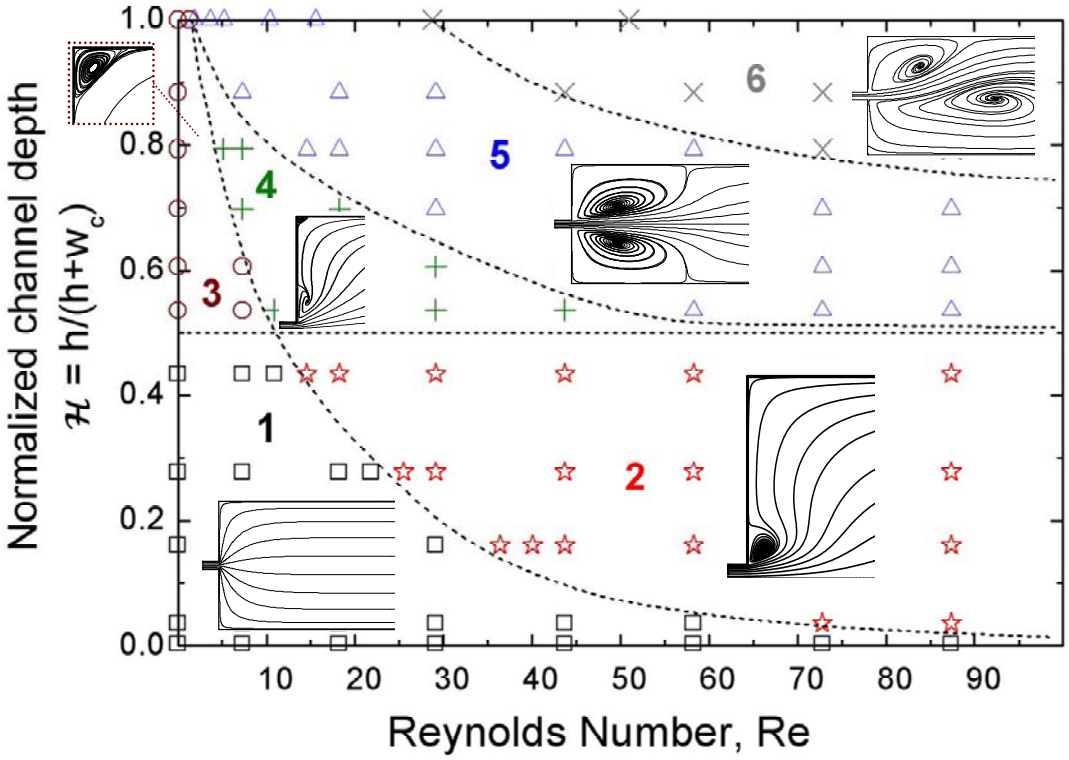

Figure11. Vortex pattern map: 1. no vortex; 2. lip vortex; 3. corner vortex; 4. lip and corner vortices; 5. full corner vortex; 6. asymmetric flow.

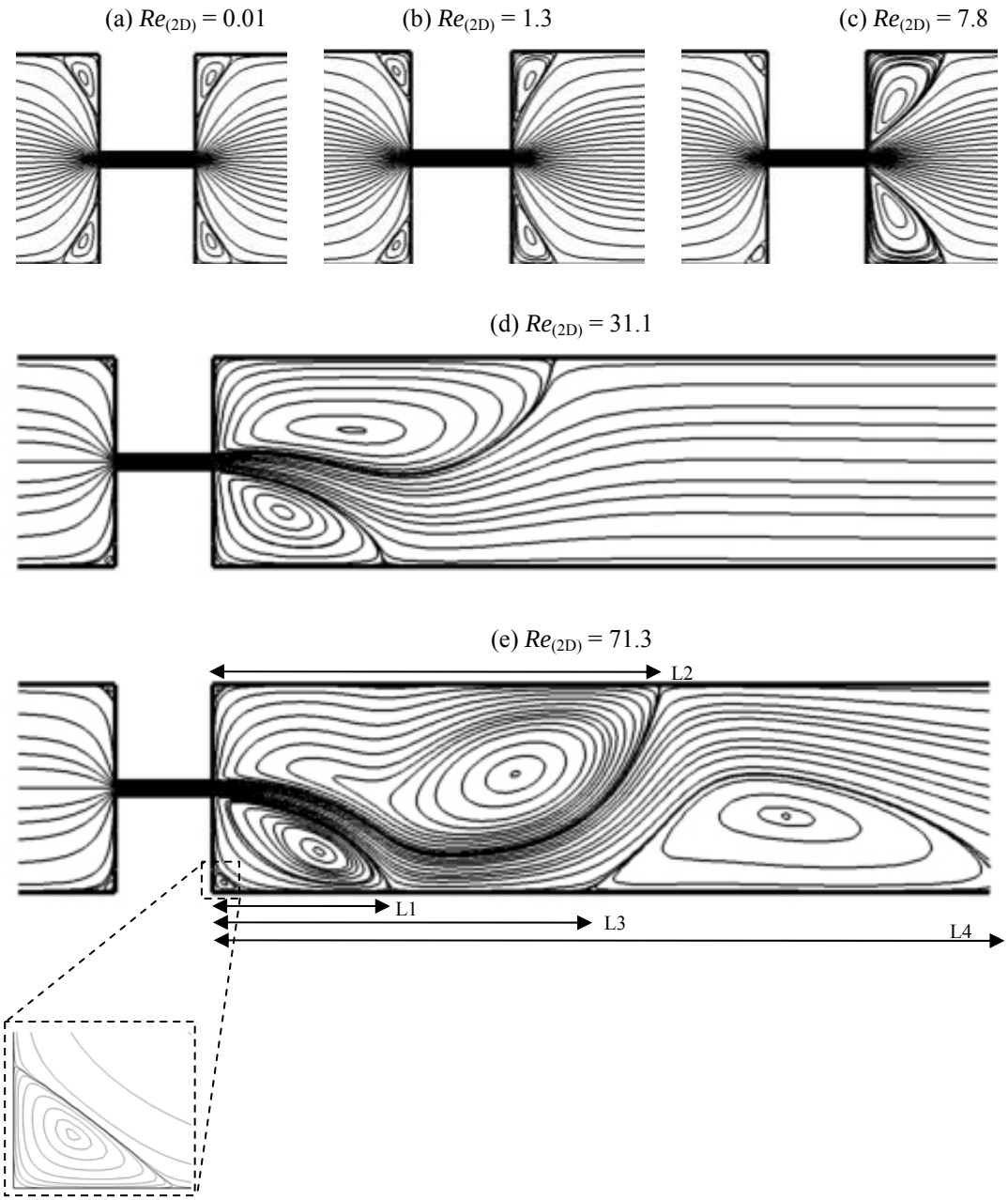

Figure 12. Predicted streamlines for a 2D contraction-expansion ($\mathcal{H}$ = 1), with w_c = 26 μm and L_c = 200 μm, over a range of Reynolds numbers: $0.01 \leq Re_{(2D)} \leq 71.3$.

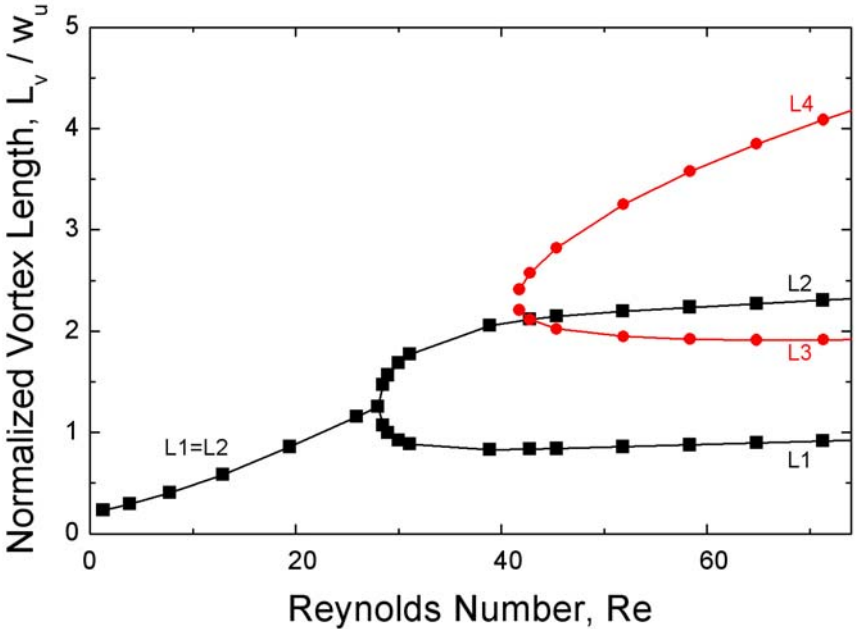

Figure 13. Bifurcation diagram for a 2D geometry ($\mathcal{H}$ = 1) with w_c = 26 μm and L_c = 200 μm: Effect of Reynolds number.

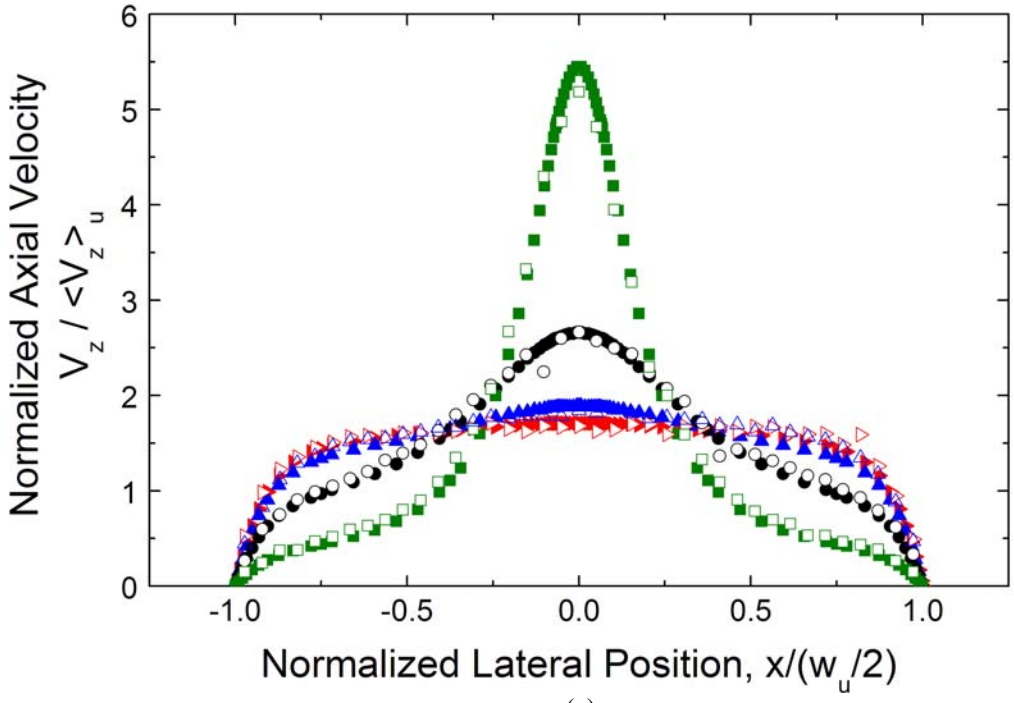

(a)

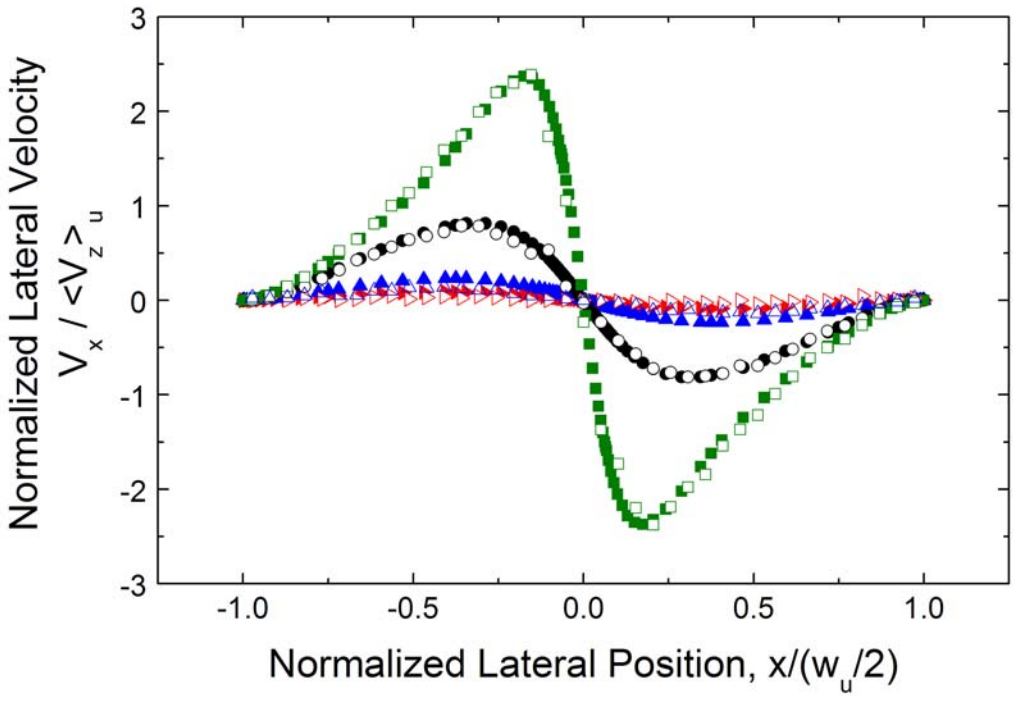

(b)

Figure 14. Comparison of the dimensionless velocity profiles at the centre plane ($y = 0$) for the contraction-expansion geometry (w_c = 26 μm, h = 55 μm) determined experimentally (open symbols) and numerically (filled symbols), as a function of the distance from the centerline for Q = 1ml/h and a range of z-positions upstream of the contraction plane denoted by the following dimensional and dimensionless positions: $z\ \left(z/(w_u/2)\right)$: (□) -47 μm (-0.235), (○) -98 μm (-0.49), (△) -195 μm (-0.975), (▷) -298 μm (-1.49). (a) Axial velocity; (b) Lateral velocity.

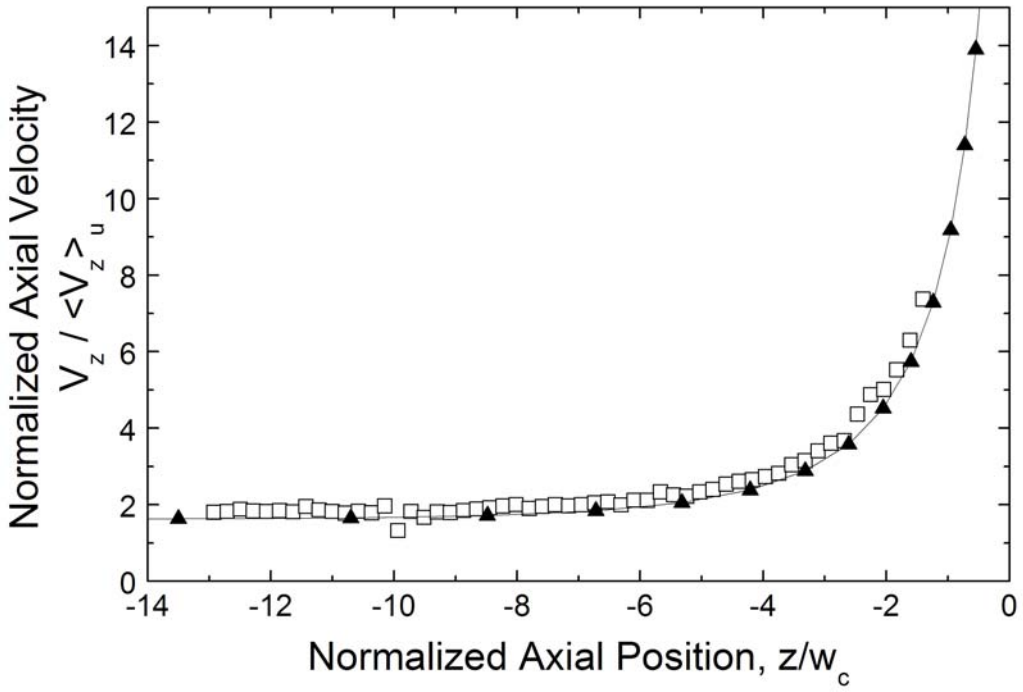

Figure 15. Axial velocity profile along the centerline ($y = 0$, $x = 0$) for the contraction-expansion geometry ($w_c = 26$ μm, $h = 55$ μm) as a function of the axial position ($-14 < z / w_c < 0$) for $Q = 1$ ml/h: experimental (open symbols) and numerical (filled symbols).

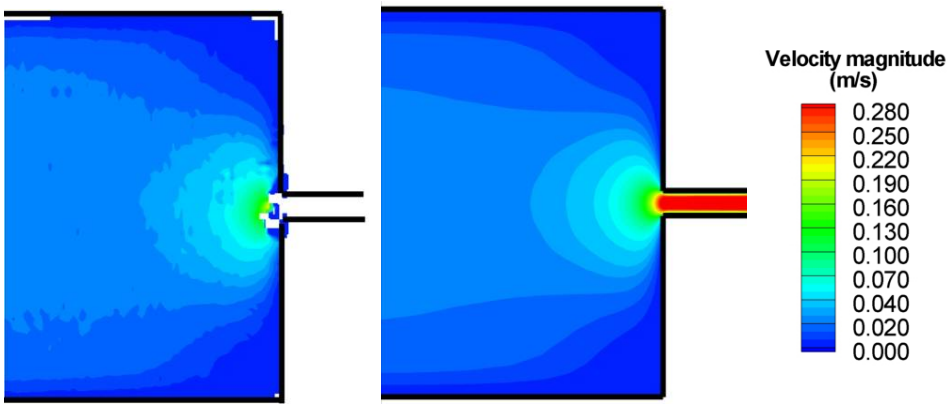

Figure 16. Velocity magnitude contour plots at the center plane ($y = 0$) near the contraction at $Q = 1$ ml/h for the geometry used in the experiments ($w_c = 26$ μm, $h = 55$ μm). (a) Experimental results; (b) Numerical predictions.

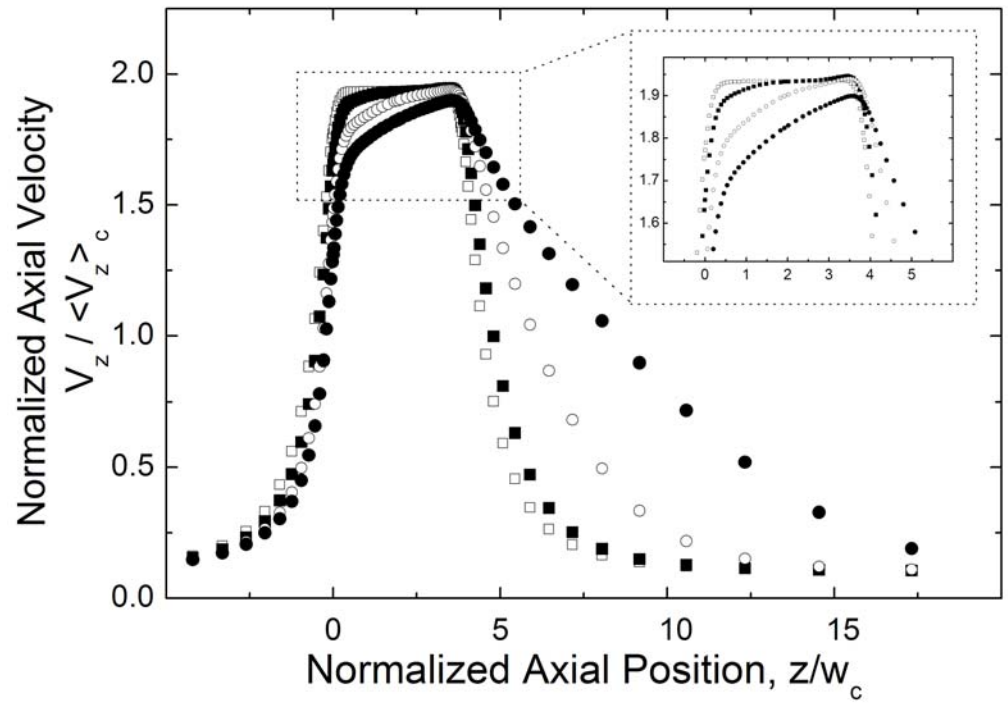

(a)

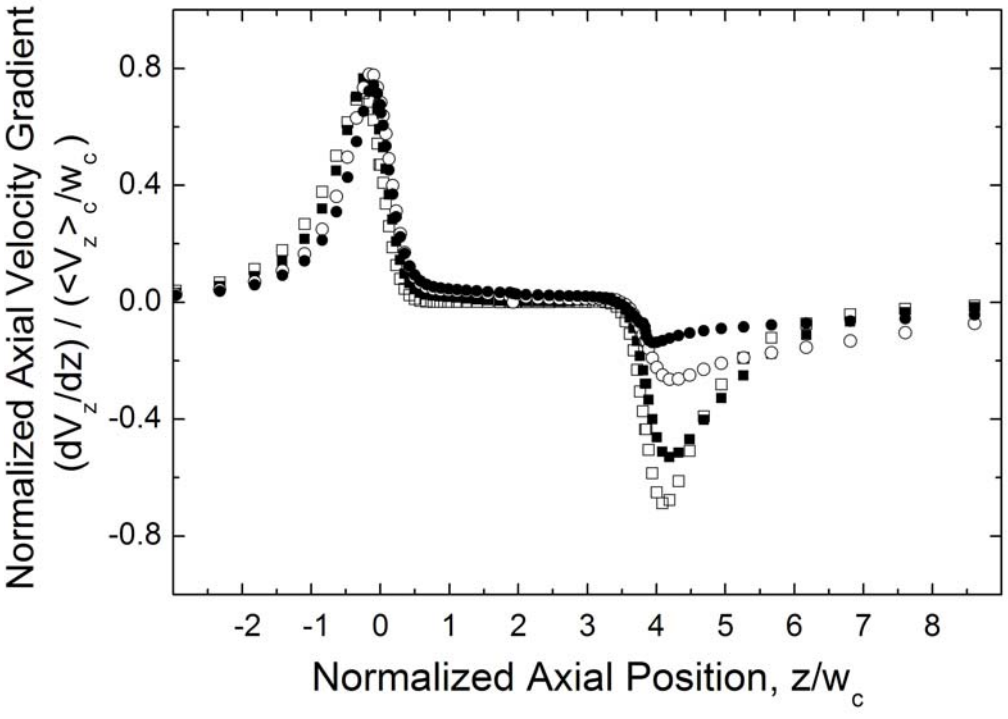

(b)

Figure 17. Predicted axial velocity profiles (a) and corresponding strain rate profiles (b) along the centerline ($y = 0$, $x = 0$) for $w_c = 26$ μm, $h = 55$ μm and $L_c = 100$ μm and a range of flow rates: $Q = 0.1$ ml/h ($Re = 0.73$) (□),$Q = 1$ ml/h ($Re = 7.3$) (■),$Q = 3$ ml/h ($Re = 21.8$) (o) and $Q = 6$ ml/h ($Re = 43.7$) (●).

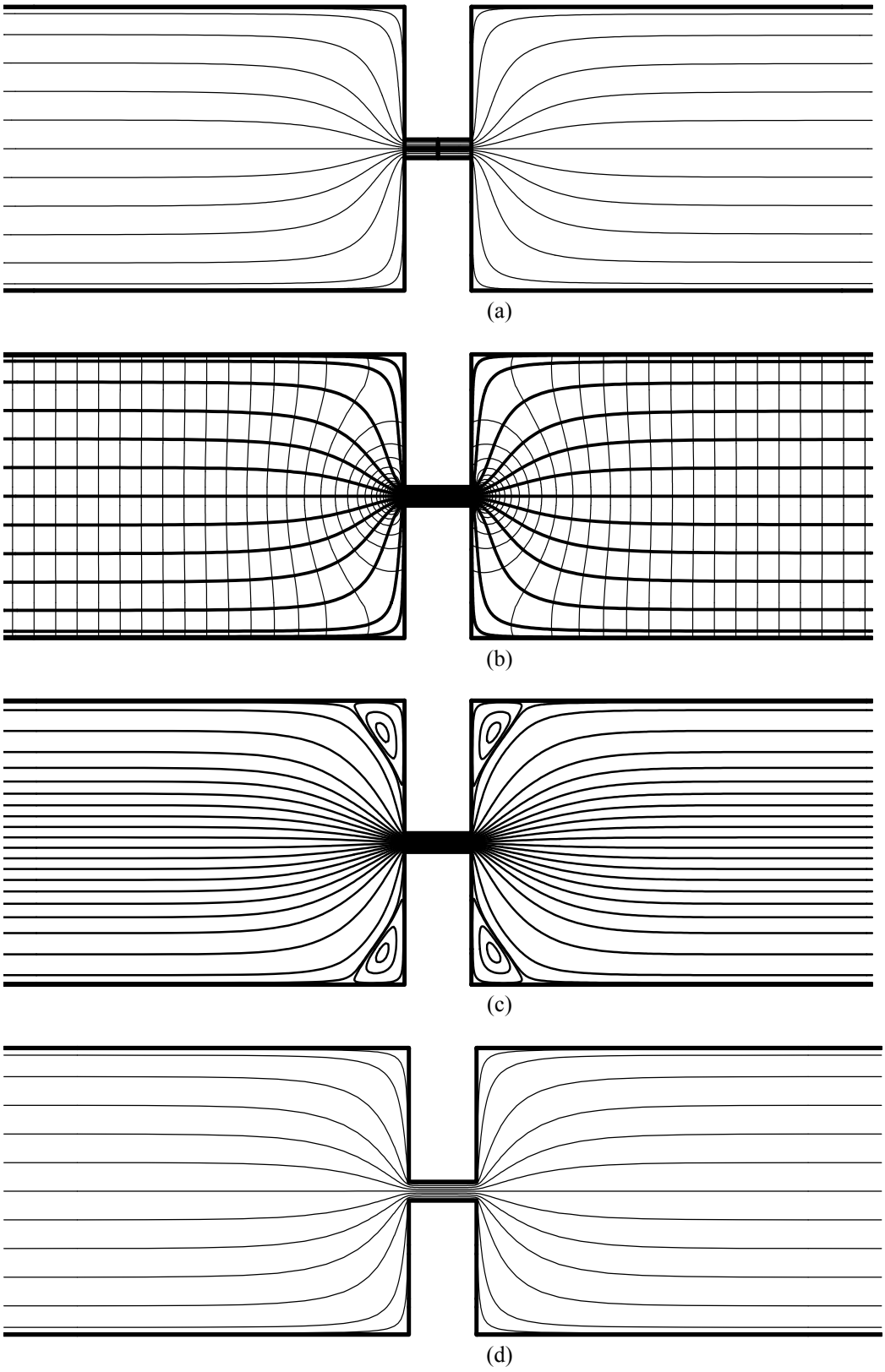

Figure 18. (a) Predicted streamlines at the centre plane ($y = 0$) for a 400:26:400 contraction-expansion with $h = 55$ μm, $L_c = 100$ μm and a flow rate of 0.1 ml/h ($Re = 0.73$). (b) Corresponding isobars (thin lines) superimposed onto the predicted streamlines (thick lines). (c) Predicted streamlines for a 2D creeping flow. (d) Predicted streamlines for 2D potential flow.

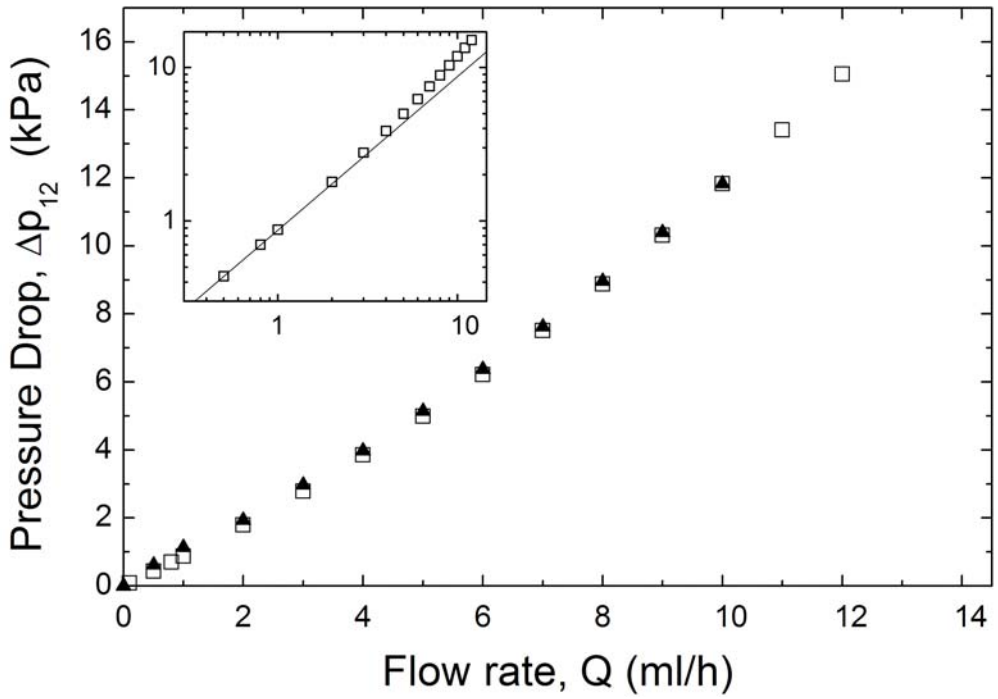

Figure 19. Comparison of the total pressure drop determined experimentally (filled symbols) and numerically (open symbols) as a function of the flow rate. The inset shows the numerical results on a log-log scale and compares the computed values with the linear behavior anticipated at low flow rates (solid line).

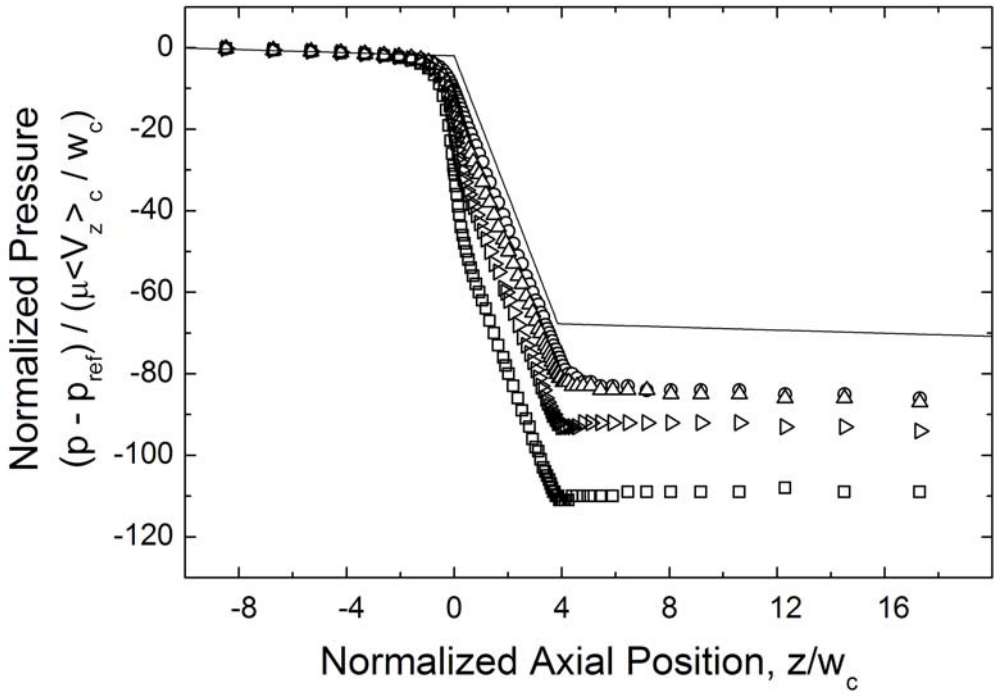

(a)

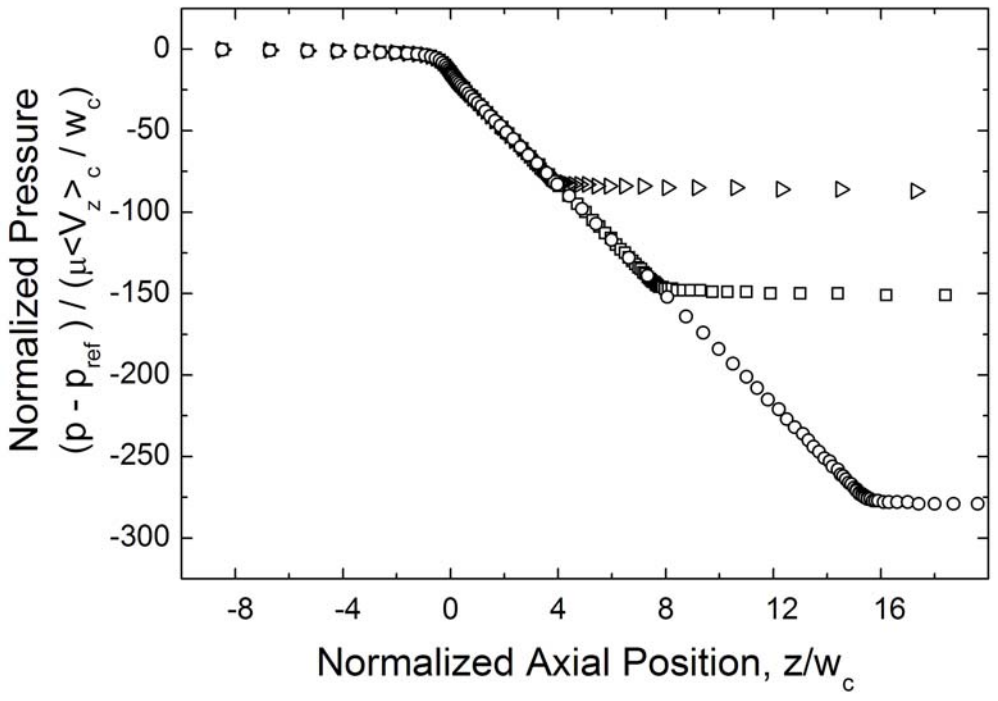

(b)

Figure 20. Normalized pressure profiles along the centerline ($y = 0$, $x = 0$) for the 400:26:400 contraction-expansion geometry with $h = 55\mu m$. (a) Effect of flow rate for $L_c = 100$ μm and $Q = 0.1$ ml/h ($Re = 0.73$) (o), $Q = 1$ ml/h ($Re = 7.3$) (Δ), $Q = 3$ ml/h ($Re = 21.8$) (▷) and $Q = 6$ ml/h ($Re = 43.7$) (□); the solid line corresponds to a hypothetical pressure profile if there were no entrance or exit effects and the flow was locally fully-developed at all times. (b) Effect of contraction length for $Q = 1$ ml/h ($Re = 7.3$) and $L_c = 100$ μm (▷), $L_c = 200$ μm (□) and $L_c = 400$ μm (o).

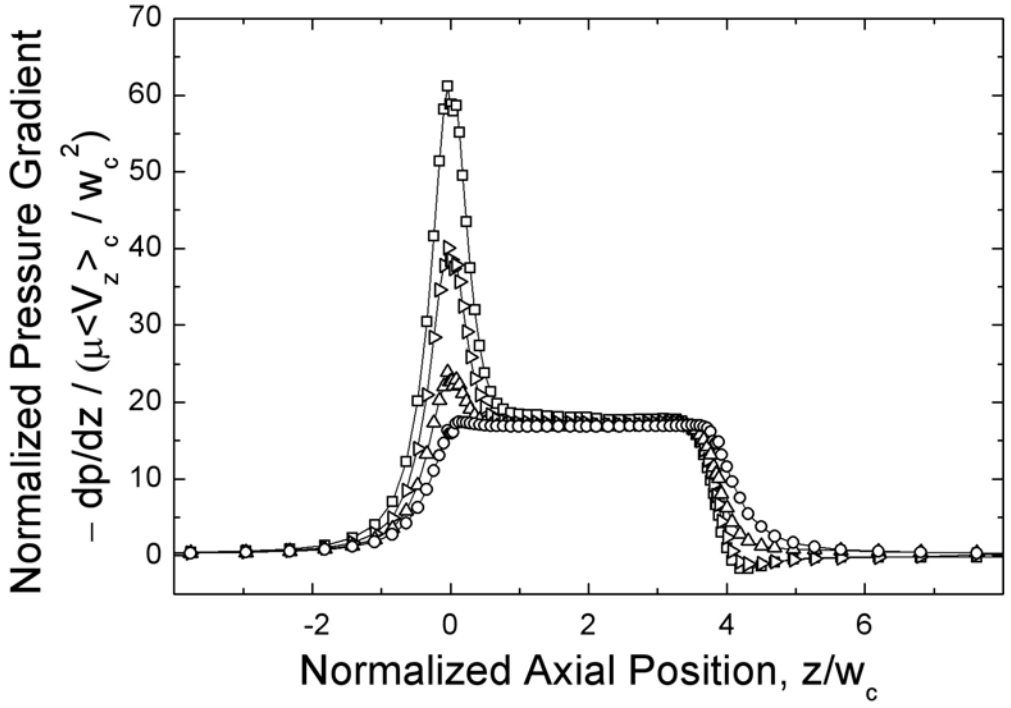

Figure 21. Normalized axial pressure gradient along the centerline ($y = 0$, $x = 0$) for $w_c = 26$ μm, $h = 55$ μm, $L_c = 100$ μm and $Q = 0.1$ ml/h ($Re = 0.73$) (o), 1 ml/h ($Re = 7.3$) (Δ), 3 ml/h ($Re = 21.8$) (⊳) and 6 ml/h ($Re = 43.7$) (□).

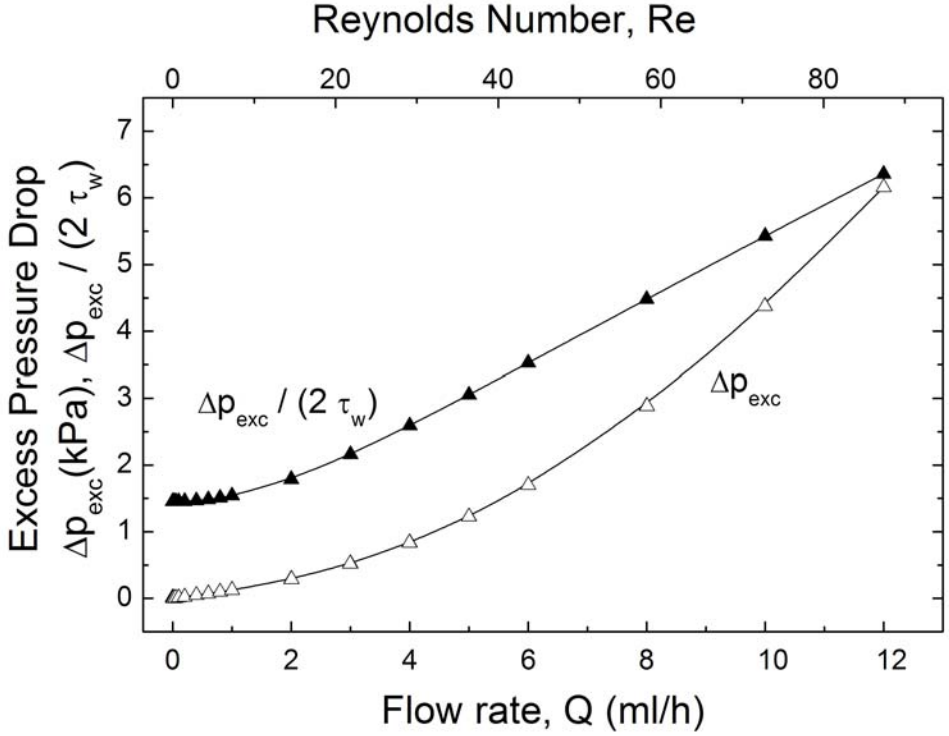

Figure 22. Effect of inertia on the excess pressure drop for a contraction-expansion geometry with w_c = 26 μm, h = 55 μm and L_c = 400 μm.

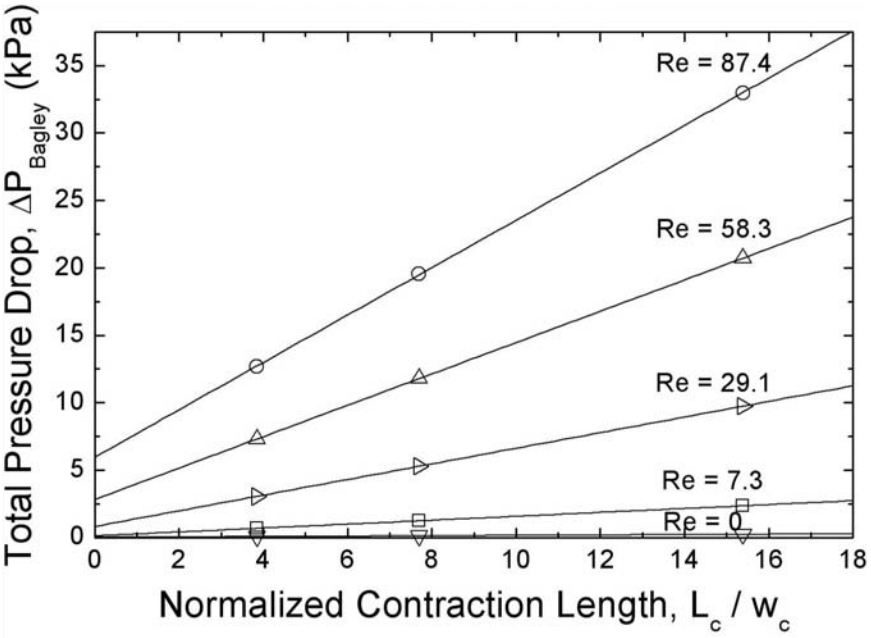

Figure 23. Bagley plot for a range of Reynolds numbers ($Re \leq 87.4$) in the 400:26:400 contraction-expansion geometry with $h = 55$ μm.

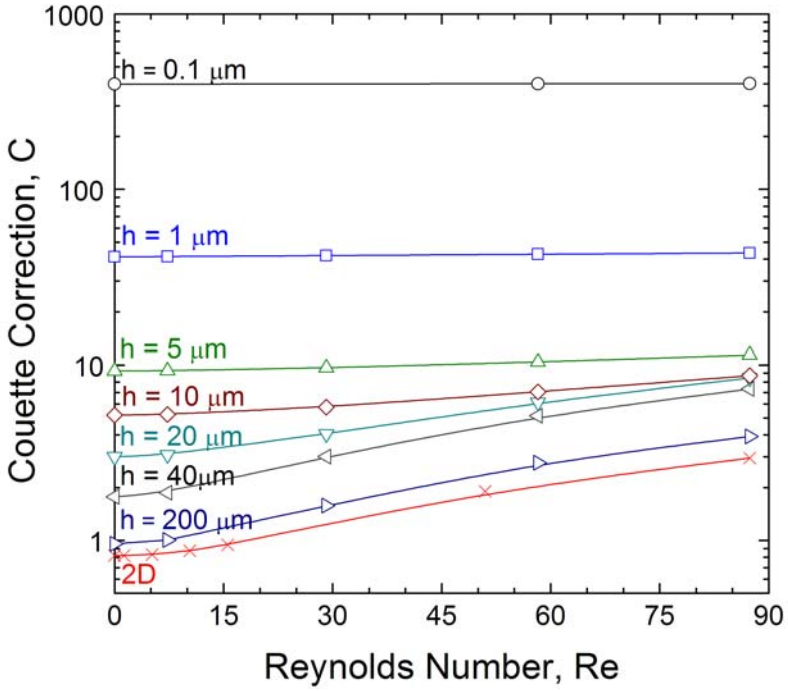

(a)

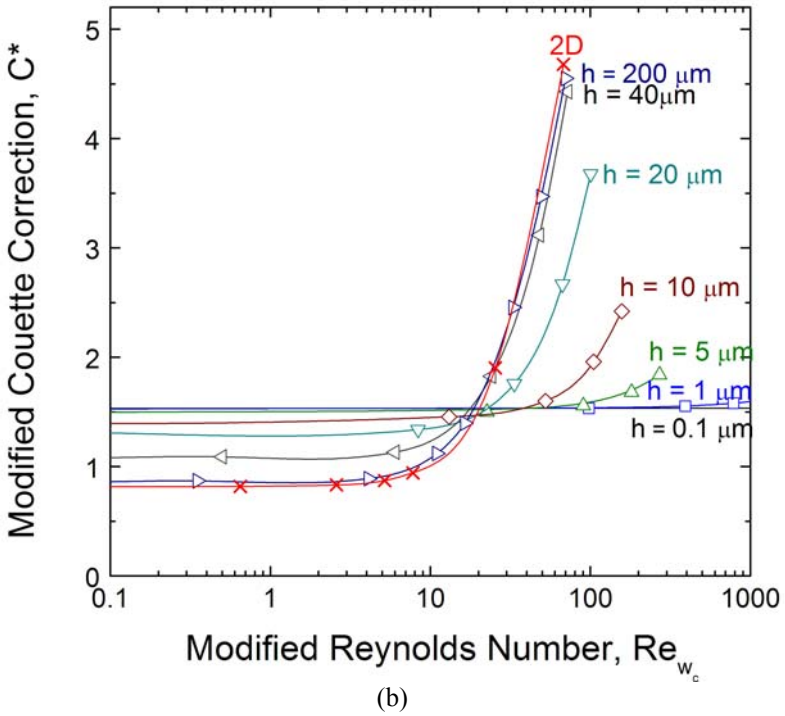

(b)

Figure 24. Effect of the aspect ratio on the standard (a) and modified Couette correction (b) for the 400:26:400 contraction–expansion geometry: h = 0.1 μm ($AR = 3.85\times10^{-3}$); h = 1 μm ($AR = 3.85\times10^{-2}$); h = 5 μm ($AR = 1.92\times10^{-1}$); h = 10 μm ($AR = 3.85\times10^{-1}$); h = 20 μm ($AR = 7.69\times10^{-1}$); h = 40 μm ($AR = 1.54$); h = 200 μm ($AR = 7.69$); 2D ($AR \rightarrow \infty$)